Università degli Studi di Napoli Federico II

Scuola Politecnica e delle Scienze di Base

Dipartimento di Scienze della Terra, dell'Ambiente e delle Risorse (DiSTAR)

DOTTORATO DI RICERCA IN SCIENZE DELLA TERRA, DELL'AMBIENTE E DELLE RISORSE

XXXVII cycle

Facing ambiguity in potential fields modelling with inverse-theory and AI algorithms

Supervisor

Ch.mo Prof. Maurizio Fedi

Candidate

Luigi Bianco

Foreign Tutor

Dr. Ed K. Biegert

(Former Shell; Rice University)

PhD-Coordinator

Ch.mo Prof. Luigi Ferranti

ABSTRACT

In this work, starting from the concept of absolute and relative ambiguities, I studied the behaviour of ambiguities in potential fields and possibilities of reducing it via multiscale methods of imaging, inversion and Machine Learning. Through a careful multiscale analysis of the fields generated by the two sources, I defined the existence of a region of ambiguity and a region in which the sources could be distinguished. The multiscale inhomogeneous properties of the fields due to general sources were adopted to generalize the imaging method called Depth from Extreme Points (DEXP) in the Inhomogeneous DEXP (INDEXP).

Then, proposed a new approach on joint inversion of gravity data for dealing with the ambiguity due to the field of vertically-stacked sources. It is based on the sequential joint inversion with cross-gradient constraint applied to gravity field and its second-order vertical derivative so resulting in a Multi-Order Sequential Joint Inversion (MOSJI). In this way, I wanted to exploit the different wavenumber-contents of the two dataset to reliably model sources at different depths.

The opportunities represented by the use of a sequential strategy lit the idea of performing a two-step joint inversions workflow for cross-gradient constrained inversion of gravity data with seismic models. The proposed method avoids the computationally-expensive seismic inversion and recover a final density model which fits the gravity measurements and presents structural features from the seismic model. The final density model which images both the main bodies and the background is also able to provide information to update and improve seismic models.

Finally, I studied the ambiguity generated by the need of a synthetic training set in supervised ML methods. For this reason, I proposed to generalize the training set of ML algorithm with a set of simple sources, the so-called building blocks, and their gravity anomalies (FaultNet3D). This is possible under the assumption that complex geometries could be analysed by a CNN as the ensemble of the gravity

anomalies generated by the edges. However, to preserve the validity of the assumption it requires the interpretation of 2D gravity data (e.g., extracted profiles from gravity maps). To overcome this limitation, I merged 2D interpretations into a reference model to constrain a 3D gravity inversion, so constituting a “self-constraint".

All the synthetic tests and real case applications were selected to target the United Nation Sustainable Development Goals (UN SDG), including energy transition, environmental safety and hazard assessment.

INTRODUCTION

The need to face and effectively reduce interpretative ambiguities affects all geophysical methods in different ways (Roy, 1962). Among them, potential fields methods are well-known to suffer from non-uniqueness of solution.

In fact, the inverse problem of finding the model m from the measured data f has inherently ambiguous solutions due to the Greens' third identity and infinite different source distributions could reproduce the same field (Blakely, 1996). Equivalently, we may say that the source distribution which results in the so-called annihilator of the equation system relating the data to the model could not be determined (Parker, 1977).

In addition, other kinds of ambiguities arise from different aspects that affect data acquisition and modelling, so toughening the interpretation of potential fields. For instance, Fedi et al. (2005) suggests to distinguish among different types of ambiguity:

- the data-error ambiguity, which is due to the instrumental and experimental errors that are produced by the characteristics of the deployed instrument and to numerical errors induced by the processing techniques;
- the sampling ambiguity, that is due to the practical limitations of having a more or less dense measurement step;
- the algebraic ambiguity, which arises when an underdetermined system of equations relating the data to the model is formed by the discretization of the source parameters in more elements than the acquired measurements. This is a typical scenario in geophysical data interpretation since the underground source volume is modelled in a 3D volume with 2D data.

One important aspect to deal with ambiguity is the introduction of *a-priori* information. The simplest way to constrain the solution is the discretization of the source volume in elementary shapes (e.g., prismatic cells) each having homogeneous properties (Menke, 2018). Similarly, specific information on the characteristics of the source can be introduced (e.g., known depth-to-top from seismic interpretation or wells; expected geometries and/or physical parameters ranges from geological knowledge). These direct constraints could be used in the form of prior model or of boundaries on the physical parameters range (Li and Oldenburg, 1996, 1998; Portniaguine and Zhdanov, 2002). A softer constraint consists in the possibility to mathematically impose a desired behaviour of the source distribution. The adopted operator will drive the solutions to be smooth (Li and Oldenburg, 1996) or compact (Last and Kubik, 1983; Portniaguine and Zhdanov, 1999; Pilkington, 2009).

While the described *a-priori* information could be addressed to as external constraints, Paoletti et al. (2013) introduced the possibility to adopt useful information extracted from the fields themselves, such as depth estimates (Smith, 1959; Fedi and Florio, 2013; Bianco et al., 2024), horizontal boundaries of the causative bodies (Blakely and Simpson, 1986; Fedi, 2002) and, most importantly, the structural index N, a parameter specific of a given kind of source shape, such as sphere, dyke and so on (Reid et al., 1990; Stavrev, 1997; Cella and Fedi, 2012; Ialongo et al., 2014; Fedi, 2016a). They referred to this category of *a-priori* information intrinsically present in the field as "*self-constraints*". I refer to (Silva et al., 2001; Barbosa et al., 2002) and references therein for deeper insights into the topic of *a-priori* information.

Another way of reducing the ambiguity of the geophysical inverse problems is the so-called joint inversion techniques, aiming at modelling different datasets in combined strategies. The data could be quantities derived by a common field, such as the Newtonian potential, (Li and Oldenburg, 2000; Paoletti et al., 2016; Capriotti and Li, 2022; Bianco et al., 2024) or different geophysical data (Fregoso and Gallardo, 2009; Lelièvre et al., 2012; Sun and Li, 2016; Tavakoli et al., 2021).

Joint inversion appears to be worth of the heavy computational efforts required as they output two related models which are iteratively updated. However, this approach requires appropriate relative weights for the different terms of the objective function to be minimized. This reflects in the fact that one of these terms can take over the others and drive the process toward a non-representative model that, by the fact, is still fitting the data within a desired error. On the other hand, the process of building a constraint, such as a reference model (Liu et al., 2024), is affected by the need of strong assumptions (e.g., empirical relationship).

While joint inversion is still an open field for applied geophysicists, the recent advancements in Artificial Intelligence (AI) may provide new methods to face the ambiguity. ML methods are being increasingly developed as reliable and data-driven tools for the automated interpretation of geophysical data. In ML for applied geophysics purposes, one of the main difficulties is to get an enough generalized training dataset without incurring in the overfitting problem. This occurs when a training dataset, including only a narrow range of pairs, is not able to adequately interpret a wider range of scenarios. The lack of a sufficiently large dataset of real data and true subsurface models reflects into the common approach to generate synthetic models and compute their corresponding field.

Following the aim of the thesis, in **Chapter I**, I show that studying the potential fields with multiscale methods, such as those based in the Wavelet Domain or in the Harmonic Domain (the source-free region, in which the field is analyzed at various altitudes), may reduce the ambiguity. In particular, I studied the multiscale behaviour of the fields related to a step and a flexure and show that the ambiguity is not absolute but, fortunately, relative. To this end, I used the Multiridge method (Fedi et al., 2009) which yields information on the depth to the source at different scales and estimated the field homogeneity-degree function $n(x, y, z)$ for many positions in the harmonic region according to the inverse method of Vitale and Fedi (2020). My study about the relative ambiguity led to introduce the concept of *Region of Ambiguity*.

Finally I show that if the field is inhomogeneous, e.g., $n(x, y, z)$ is not constant, imaging techniques such as the Depth from Extreme Points (DEXP) may be reformulated by using a not constant *n* and that such *inhomogeneous DEXP* may be useful to fix the ambiguity of the step-flexure sources. The proven method was finally applied to the real case of and abandoned mine in Udden, Sweden which is of interest for environmental purposes and as a potential storage site for radioactive materials.

In **Chapter II**, I face the ambiguity generated by the anomalies due to vertically-stacked sources (e.g., salt dome and mother salt) using the fact that vertical derivatives of the field of various order have different wavenumber-contents. To accomplish this task, I will move into the framework of cross-gradient-constrained joint inversion of the gravity field and its second-order vertical-derivative. I call the proposed workflow *Multi-Order Sequential Joint Inversion (MOSJI).* To test the method, I selected the realistic synthetic model SEG Advanced Model (SEAM) Phase I, which reproduces a salt domain in the Gulf of Mexico. It is one of the most studied scenarios for Exploration and Carbon Storage. I studied also the real case of karst cavities, posing a direct hazard on people, which is however a common example of interpretation pitfall, due to the occurrence of multiple sources at different depths.

In **Chapter III**, I will develop a new type of joint inversion workflow to accomplish the general task of combining gravity and seismic data. The originality of the method is that does not need a conversion-rule of each of the two source properties, but it is able to import the main structural features of a seismic model or even of a general geological model. To test the method, I selected again the synthetic model SEAM Phase I. Then, I modeled the Mors Salt Dome in Denmark.

Finally in **Chapter IV**, I will face the ambiguity in supervised ML methods. Since these methods intrinsically need a synthetic training set, I will formulate a strategy to build it based on the simplest source in potential fields, it is to say faults and contacts and their respective anomalies. From this, I will produce ML interpretations that are then refined via 3D inversion. The ML algorithm was tested on a synthetic model representing a salt dome-like structure. Finally, I applied the method to the reconstruction of the Caltanissetta Basin from gravity data via such ML algorithm. This last representing a typical basin-scale geophysical modelling which can applied to many situations for different purposes.

I want to underline that the modelled scenarios were selected as they are targeting the United Nations Sustainable Development Goals (UN SDG) in different areas from energy transition to environmental and hazard assessment. Thus, the proposed methods represent important tools in the path to the UN-SDG.

1 AMBIGUITY IN POTENTIAL FIELDS

2 Multi-order joint inversion of gravity data with inhomogeneous depth weighting

This chapter is from: Multi-Order Sequential Joint Inversion of gravity data with inhomogeneous depth weighting: from near surface to basin modelling applications; Bianco L., Tavakol M., Vitale A., Fed M.; 2024; IEEE Transactions on Geosciences and Remote Sensing.

The deeper understanding of ambiguities in potential fields modelling is crucial to address the problem of facing relative ambiguities via AI algorithms. In fact, unless simple cases involving a single source, potential field anomalies are produced by the superposition of different source contributions, which interfere each other. Thus, many methods address the inversion problem by first separating the effects of sources seated at different depths, but this is one of the trickiest tasks in potential fields modelling. In general, standard filters often do not accomplish satisfactorily this task, mainly because they are merely mathematical tools applied to physical signals. Instead, physically-based transformations, such as upward continuation or differentiation may be more useful.

In this framework, one could invert single components of the GGT (e.g., G_{zz}) or combinations of them (Li, 2001; Zhdanov et al., 2004; Martinez and Li, 2011). Different authors have explored these opportunities. Biegert et al. (2001) found that G_z and GGT inversion could be used to define the thickness of the salt and its top, respectively. Capriotti and Li (2014) developed an algorithm to jointly invert G_z and GGT adopting a unique data misfit. They achieved improved solutions at depth when compared to inverting only the gravity gradient data for a simple block and a basin-like test. Paoletti et al. (2016) performed a joint inversion on the Vredefort Crater and analyzed its performance through a singular value analysis. Capriotti and Li (2022) jointly inverted gravity and gravity gradient fitting each dataset at its own noise level. They adopted a weighting parameter among the different parts of an enlarged data misfit and obtained improved models in basin-like tests. Although the actual improvement brought by jointly inverting gravity and gravity gradients data is still debated, one can address this topic by looking at both the positive and negative findings already mentioned.

To fully exploit the different wavelength-contents of the vertical derivatives of the field or the different information brought by the seismic and the gravity, it is worthy to find an appropriate strategy not to combine all the data into a unique data misfit. This leads to the strategy of treating them as two separate datasets and combining resulting models via a structural constraint called cross-gradient constraint.

The cross-gradient constraint was firstly introduced by Gallardo and Meju (2003) and has been applied to jointly invert different geophysical datasets to the end of enforcing the structural similarity of the different physical properties. Fregoso and Gallardo (2009) were the first to develop a cross-gradient joint inversion of magnetic and gravity data. Later, Um et al. (2014) introduced a coupled inversion of large-scale seismic and electromagnetic data for subsalt imaging. It can be seen as a sequential approach including the cross-gradient constraint term. They split the joint inversion into separate EM, seismics and cross-gradient inversions. This latter allows to constrain the resistivity model based on a reference velocity model. The resulting resistivity model will serve as initial model for a new EM separate inversion in an EM refinement process. The approach aimed at an easy minimization of the cross-gradient term. However, the cross-gradient minimization could worsen the data fitting. In the subsequent iteration, the data misfit will be minimized in separate inversions, which could indeed produce a lower structural similarity. Gao and Zhang (2018) proposed a strategy to avoid this behaviour using the model perturbations resulting from stand-alone inversions to constrain the cross-gradient minimization at each iteration. Gross (2019) introduced an algorithm for a weighted joint inversion of gravity and magnetic data using again a cross-gradient constraint. He achieved an improved structural similarity of the models thanks to a local weighting of the cross-gradient. Zhang and Wang (2019) introduced a joint inversion based on structural coupling. They adopted a fast gradient algorithm to solve the objective function, which was composed by three terms: the data misfit, the cross-gradient and the total-variation regularization constraint. This latter led to a more focused and sharp solution.

Tavakoli et al. (2021) introduced a sequential workflow for the joint inversion of gravity and magnetic data and obtained a successful modelling of evaporite structures. Fang et al. (2022) extended the sequential approach to a 3D joint inversion of gravity and magnetic data. Other authors (Zhang et al., 2021; Meng et al., 2022; Vatankhah et al., 2022) proposed different approaches to perform a cross-gradient joint inversion of gravity and magnetic data. The sequential approach gives the opportunity to gather structural information from the different components of the field (e.g., gravity and GGT) or, as mentioned above, from gravity and seismic models.

In the multi-order joint inversion workflow, I take advantage from gravity and its q^{th} order vertical derivatives, since they enhance different contents at medium-to-large wavelengths and at medium-to-short wavelengths, respectively. The two components of the gravity data are jointly inverted via the cross-gradient constraint in a workflow that provides the possibility of incorporating different constraints.

Among the huge variety of real-world cases of vertically-stacked sources, I chose to face that of salt basins (e.g., SEAM Phase I model) and that of karst cavities at different levels. These scenarios fall within the UN SDG as the former represent important basins for energy transition and environmental purposes (e.g., underground gas storage and waste disposal) while the latter pose immediate and unveiled hazard to social communities.

2.1 Sequential Joint Inversion via cross—gradient constraint

Gallardo and Meju (2003) defined the cross-gradient constraint between two physical properties at a given point (x, y, z) with positive z -axis pointing downward as:

$$\boldsymbol{\tau}\,(\rho, q) \;=\; \nabla\rho\;(x, y, z) \;\times\; \nabla q\;(x, y, z) \tag{2.1}$$

where ρ and q are two physical properties. In a two-dimensional case only the τ_y of the cross-gradient exists as the x - and z -components vanish.

The cross-gradient constraint is added as a penalty term to the objective function (Gallardo and Meju, 2011). In this case, the combined objective function for the joint inversion of two datasets is:

$$\psi\,(\rho, q) \;=\; \varphi_1(\rho) \;+\; \varphi_2(q) \;+\; \chi(\rho, q) \tag{2.2}$$

where $\varphi_1(\rho)$ and $\varphi_2(q)$ contains the data-misfit and the model-norm terms for each dataset; $\chi(\rho, q)$ is the norm of the cross-gradient; subscripts 1 and 2 refer, respectively, to the two different datasets; ρ and q are the two different physical parameter vectors.

Following the purpose of this section I now rewrite (2.1) as:

$$\boldsymbol{\tau}\,(\rho_1, \rho_2) \;=\; \nabla\rho_1\;(x, y, z) \;\times\; \nabla\rho_2\;(x, y, z) \tag{2.3}$$

where ρ_1 and ρ_2 refer to density models recovered from the gravity and the gravity gradient respectively.

Equation (2.2) becomes:

$$\psi\,(\rho_1, \rho_2) \;=\; \varphi_1(\rho_1) \;+\; \varphi_2(\rho_2) \;+\; \chi(\rho_1, \rho_2) \tag{2.4}$$

where $\varphi_1(\rho_1)$ and $\varphi_2(\rho_2)$ are the gravity and gravity gradient data objective functions and $\chi(\rho_1, \rho_2)$ is the 2D cross-gradient.

At each j^{th} iteration the model perturbations $\Delta\boldsymbol{\rho}_{1j}$ and $\Delta\boldsymbol{\rho}_{2j}$ are determined via separate inversions and used to constrain the cross-gradient term minimization. The system for the joint inversion of two datasets through the minimization of the cross-gradient term $\chi(\rho_1, \rho_2)$ is after (Gao and Zhang, 2018):

$$\begin{bmatrix} \mathbf{I} & 0 \\ 0 & \mathbf{I} \\ \mathbf{t_1} & \mathbf{t_2} \end{bmatrix} \begin{bmatrix} \Delta\hat{\boldsymbol{\rho}}_{1j} \\ \Delta\hat{\boldsymbol{\rho}}_{2j} \end{bmatrix} = \begin{bmatrix} \Delta\boldsymbol{\rho}_{1j} \\ \Delta\boldsymbol{\rho}_{2j} \\ -\boldsymbol{\tau} \end{bmatrix} \tag{2.5}$$

where **I** is the identity matrix; $\mathbf{t}_1$ and $\mathbf{t}_2$ are the partial derivative matrices ($\partial\tau/\partial\rho_1$ and $\partial\tau/\partial\rho_2$, respectively) of the 2D cross-gradient. The solutions of (2.5) are the cross-gradient constrained model perturbations $\Delta\hat{\boldsymbol{\rho}}_{1j}$ and $\Delta\hat{\boldsymbol{\rho}}_{2j}$. In this way, I constrain the cross-gradient minimization with the model perturbations retrieved from separate inversions. Tavakoli et al., (2021) used this strategy as the key-step for their sequential joint inversion algorithm.

To perform the separate inversion of gravity data, I adopted the algorithm introduced in section 1.3: *inversion with inhomogeneous model depth-weighting* that is to minimize:

$$\mathbf{m} = \arg\min_{\mathbf{m}} \left\{ \|\mathbf{Am} - \mathbf{d}\|_2^2 + \mu^2 \sum_{c=1}^{M} \frac{w_c^2 m_c^2}{m_c^2 + \varepsilon^2} \right\} \tag{2.6}$$

With the model depth-weighting function:

$$w(x, y, z) = \frac{1}{z^{\left[\frac{\beta(x,y,z)}{2}\right]}} \tag{2.7}$$

2.2Joint Inversion Worfklow

I now define the workflow (see Fig. 2.1) for vertically-stacked sources modelling of G_z and its 2^{nd} order derivative G_{zzz}. Other combinations may be exploited that could involve also fractional-order derivatives (Florio et al., 2022). Prior to jointly invert my data, I proceed with the computation of the inhomogeneous depth weighting function (12). I compute $\beta(x, y, z)$ on G_z because it has a most complete set of contributions from deep to shallow sources. In addition, I can build a reference model by finding an unconstrained compact solution for G_{zzz}. It is to say I impose β=0. Letting the compactness to guide the process, I obtain a preliminary model of the shallow sources with only slight contributions from the deep-seated ones. It is possible to enhance this reference model with hard constraints from interpretation of other geophysical data or geological/direct knowledge of the area (e.g., wells, field geology, etc.). The computation of high-order derivatives could result in a rather low signal-to-noise. However, sometimes, the first-order vertical derivative G_{zz} is directly measured, especially during GGT surveys. These measurements could be very useful to obtain stable higher-order derivatives. Usually, vertical derivatives of potential fields may be computed numerically, here I adopt the stable algorithm of the Integrated Second Vertical Derivative (ISVD) procedure (Fedi and Florio, 2001). Once the two datasets are formed, I must define the a-priori information to express in the model weighting matrix **L** as specified before and then move to the joint inversion.

The workflow exploits the powerfulness of the joint inversion thanks to decoupling the minimization of the combined objective function in (4), in which the cross-gradient minimization is used as constraint on the iterative updates of the model perturbations as in (5). Thus, I can expect that the cross-gradient minimization could help to balance the gravity field inversion, which regards deep and shallow source contributions, with that of the second-order vertical derivative of gravity, which would include specially the contributions related to the shallowest sources.

I want to stress this aspect, as it represents a new point of view on the joint inversion of potential fields. Special tools will be used to make an adequate diagnostic of the validity of the model and of the joint inversion (see synthetic tests and real case sections).

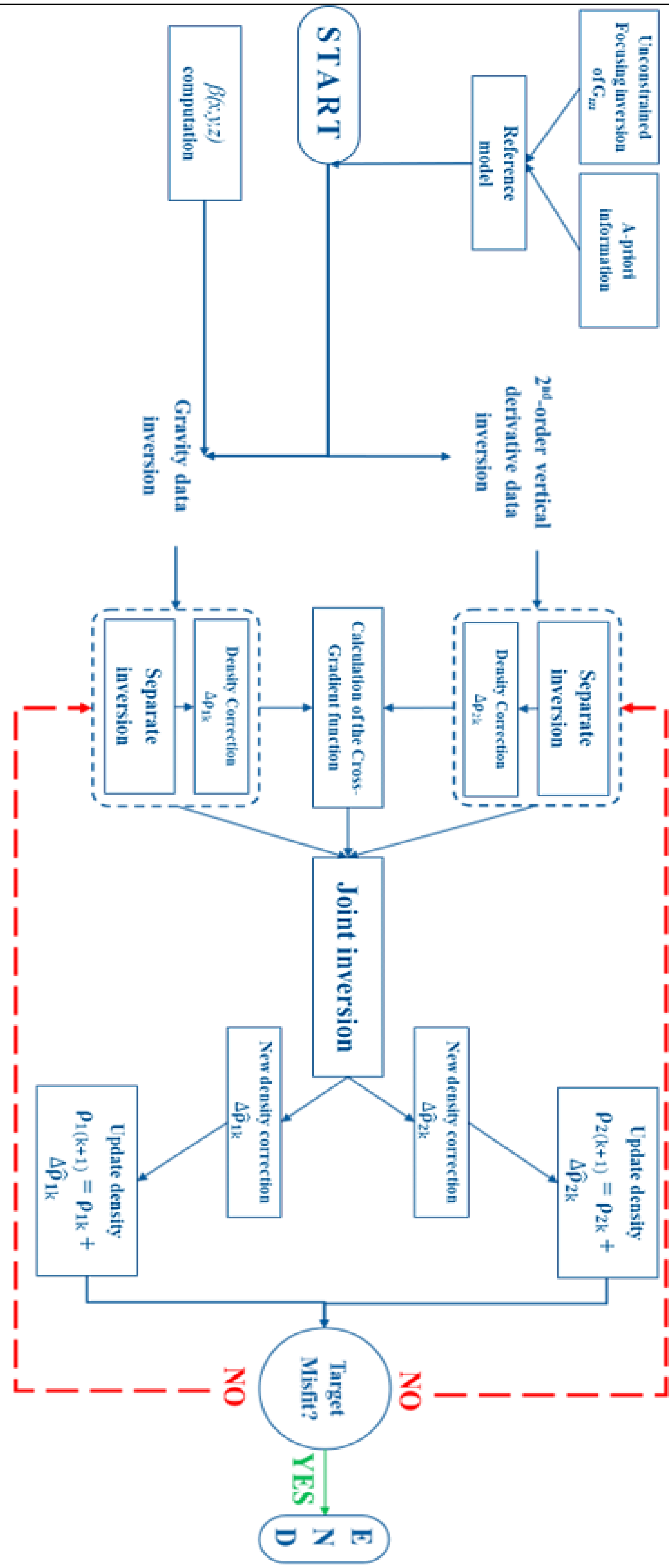

Figure 2.1: Joint Inversion Workflow

2.3 Synthetic modelling

SEAM- Phase I Model

To test my approach with a synthetic realistic model, I chose the SEAM-Phase I model (Fehler and Keliher, 2011). It is a 3D synthetic model based on a deep-water salt domain in the Gulf of Mexico. It includes a complex salt intrusive and its mother-salt in a folded Tertiary basin. The physical properties of the model and the related geophysical simulations are designed to provide key tools for testing algorithm and workflow in a realistic scenario. In fact, the model includes common challenges faced in geophysical exploration, while having a defined target to compare obtained results.

I illustrate the result obtained on the 2D profile extracted at y=4000m (Fig. 2.2d). The model consists of 135x60 cubic cells with side sizes of 250 m for a total length of 34 km and a 15 km maximum depth. The salt dome extends from 3 to about 8 km, while the top autochthonous salt layer is deeper than 12 km. Together with G_z (Fig. 2.2b), I compute G_{zzz} (Fig, 2.2a) and the inhomogeneous depth weighting function on G_z (Fig. 2.2c).

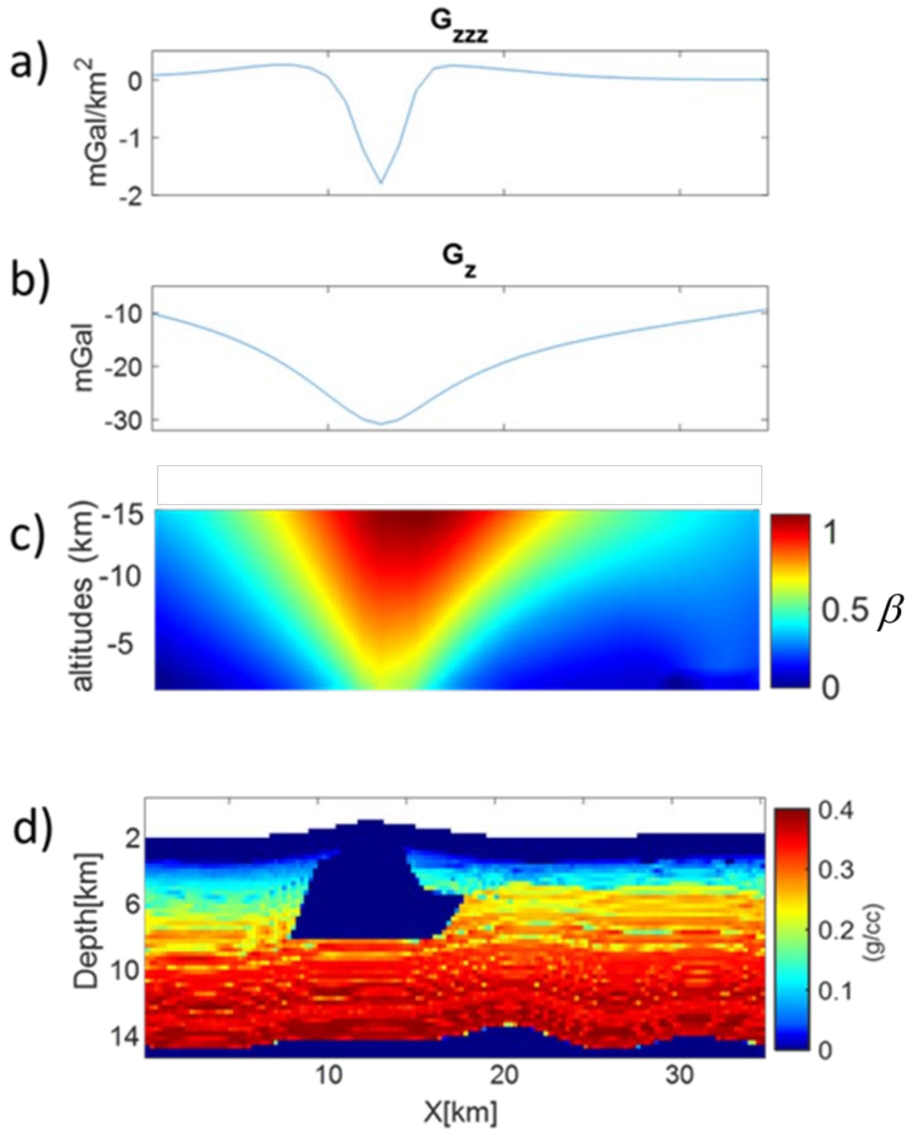

Figure 2.2: a) G_{zzz}; b) G_z; c) $\beta(x, y, z)$; d) synthetic density model.

In Fig. 2.3b, I show the result of a compact inversion of G_{zzz} under the assumption of a homogeneous β equal to 0. It is clear that the model is imaging in a reasonable way only the shallowest source. The contribution of the deep-seated source is not forced to the deeper portions of the model, but it is modelled as a diffuse source around the salt dome. Its density-contrast is very low, which is geologically unreliable. In Fig. 2.3a, it is possible to appreciate the low data misfit given by the root mean square error (RMSE). However, applying a threshold of -0.17 g/cc to the model, I may isolate better the contribution of the salt dome (Figure 2.3c) and use it as reference model in the joint inversion.

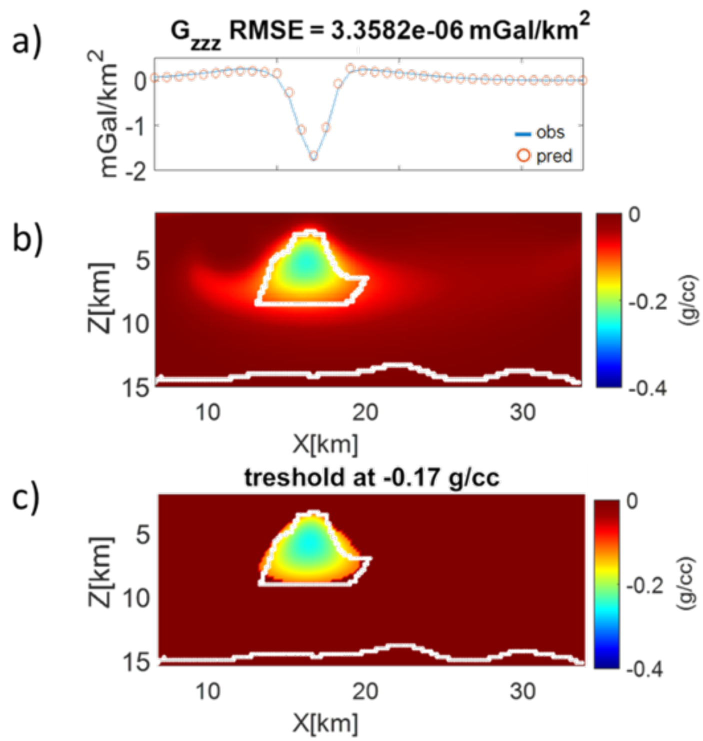

Figure 2.3: a) observed and predicted data b) G_{zzz} inversion with $\beta(x, y, z)$=0; b) model in a with an imposed threshold of -0.17 g/cc.

The results of the joint inversion are shown in Figure 2.4. I begin to describe the models resulting from separate inversions. They are clearly not able to produce an adequate modelling of the salt features. G_z inversion (Fig. 2.4a) produces a model that correctly recover an increasing density contrast with depth but joins the salt dome to the mother salt. This behavior is lost in the inversion of G_{zzz} (Fig. 2.4b), which produces a compact salt dome but with a deep root connecting it to the mother salt. Nevertheless, both models even if they have a low data misfit, they could not fix the vertical separation of the salt dome from its mother salt, which is significant in basin modelling. On the other hand, in the joint inversion, G_z

(Fig. 2.4d) is more able to retrieve a rather complete model of the investigated subsurface volume while I can see that G_{zzz} (Fig. 2.4e) produces a model with only the shallower source modelled in a proper way, while targeting comparable values of data misfit to those of separate inversions. The convergence plots of joint inversion (Fig. 2.4f) are comparable to those of the separate inversions. These plots demonstrate a similar computation efficiency while including more constraints which lead to more reliable solutions.

As obvious, one of the improvements is the enhanced structural similarity in the joint inversion models. In fact, looking at the magnitude of cross-gradient values of the separately inverted models, jointly inverted models (Fig. 2.5a-b), it is possible to appreciate a strong decrease in the absolute values. It is also useful to compare the arrangement of these values. While the separate inversions show values which distribute on the whole space from the position of the shallow-seated source towards depth, in the joint inversion models they are concentrated at the boundaries of the shallower source, meaning that only details due the discretization of the model-space can be reviewed.

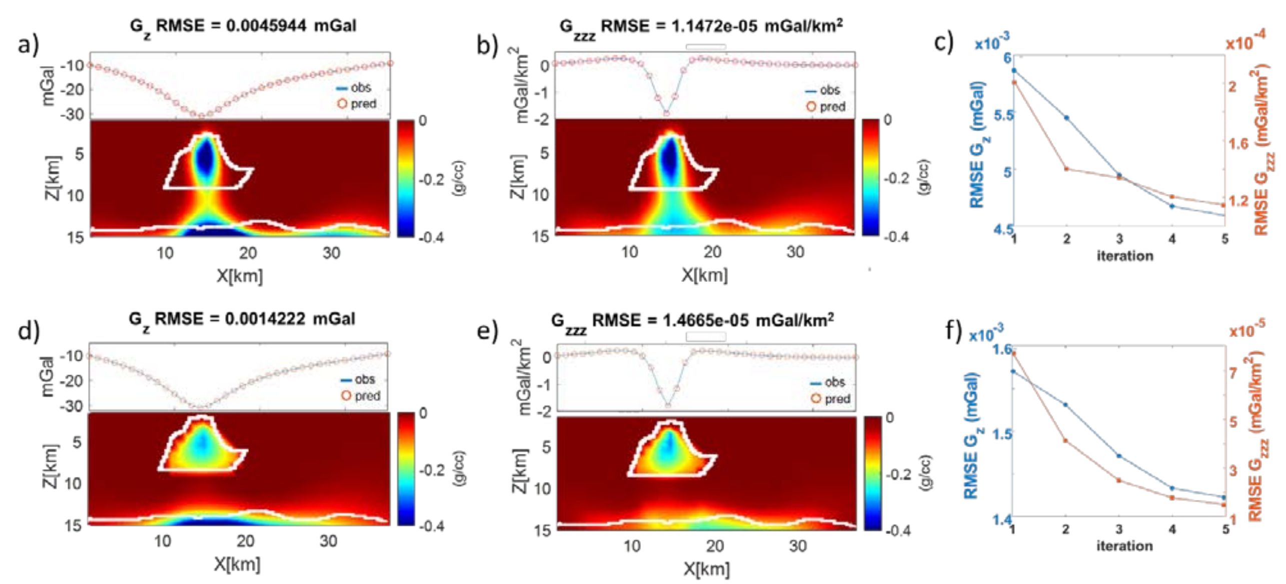

Figure 2.4: model resulting from a) separate inversion of G_z; b) separate inversion of G_{zzz} ; c) convergence plots for separate inversions d) MOSJI on G_z; e) MOSJI on of G_{zzz}; f) convergence plots for joint inversion.

An insightful result is obtained when looking at the scatter plots of the recovered physical parameters. It is possible to appreciate the linearization of the values in the jointly inverted models (Fig. 5d) with respect to common separate inversions (Fig. 5c). I can describe a diagonal linear cluster. This diagonal trend has a differentiated behaviour in its final portion. In fact, some values with lower values in the G_z model assume a higher value in G_{zzz}. This is because the sensitivity of G_{zzz} is addressed toward the salt dome, which cause less accuracy of modelling the mother salt. It is important to note that the salt dome has an average density contrast of -0.2 g/cc. For layered models, this is justified as the retrieved density distribution takes the meaning of an equivalent density contrast. It is to say that I have an actual density contrast varying with depth, but I recover from inversion a value close to the weighted mean. This concept was introduced to describe an equivalence between a stratified basin and a basin having the same shape but filled homogeneously with an average density (Litinsky, 1989a). The same equivalence was demonstrated in salt dome modelling with different density contrasts at the various layers (Chauhan et al., 2018).

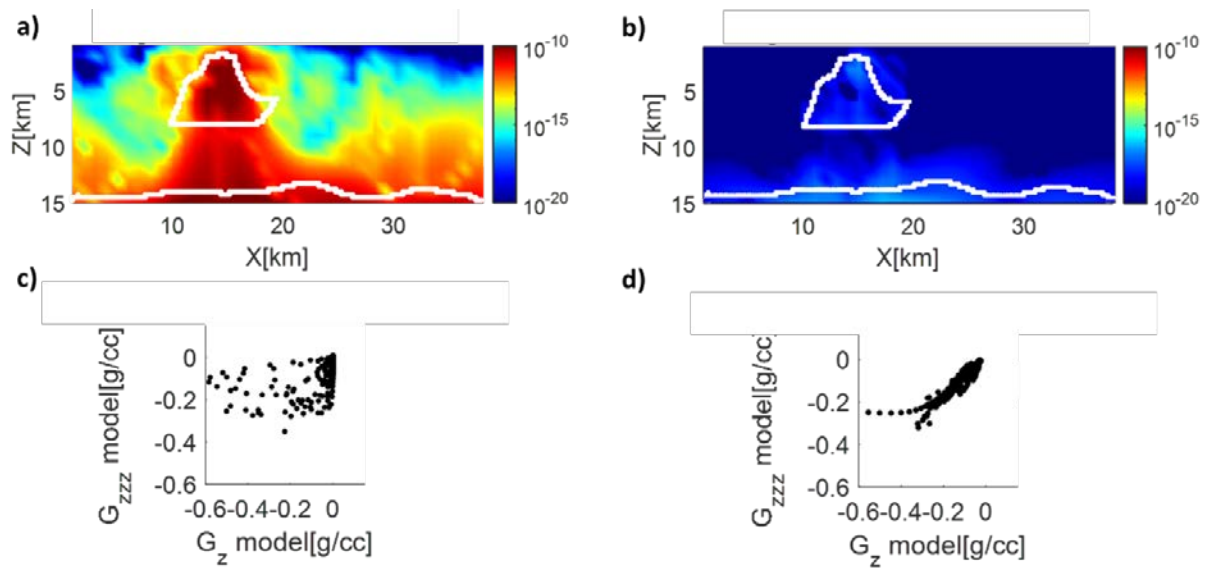

Figure 2.5: a) cross-gradients value of separate inversions; b) scatter plot of density models of separate inversions; from: c) Magnitude of cross-gradients value of MOSJI joint inversion; d) scatter plot of density models of MOSJI joint inversion.

Karst cavities model

The karst model (Fig. 2.6d) is a grid of 50x50 cells sized 2 m x 2 m. It contains two bodies at different depths. This setting represents a very complex but common challenge in karst cavities detection for hazard assessment. The density contrast between the sources and the background is set at -2.7 g/cc. The synthetic G_z (Fig. 2.6b) was computed with spacing of 2 m, while G_{zzz} (Fig. 2.6a) was obtained thanks to the ISVD method. Following the procedure described in previous section, I computed $\beta(x, y, z)$ matrix based on the G_z data (Fig. 2.6c).

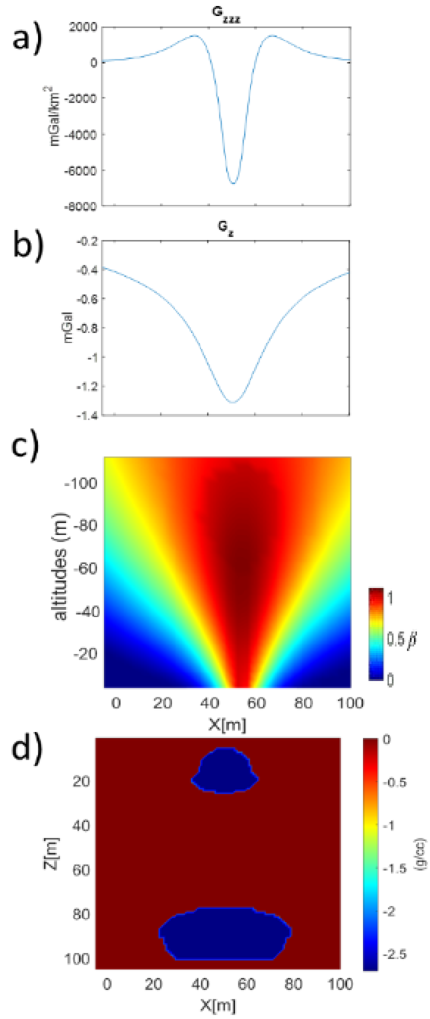

Figure 2.6: a) G_{zzz}; b) G_z; c) $\beta(x, y, z)$; d) synthetic density model.

Separate inversions do not produce a clear separation between the two sources. In the model retrieved from G_{zzz} inversion (Fig. 2.7b), the deep-seated source appears as a low-density diffuse source. At the same time, the density of the shallowest source is clearly overestimated. Model resulting from G_z (Fig. 2.7a), produce a similar model, still missing a proper density contrast, lateral extension and depth position. I can note that in this latter model, there is a slightly improved recover of the deep-seated cavity. This reflects the fact that G_z brings more information on the deepest source. In general, I can state that nor the G_z or G_{zzz} are able to recover a correct density distribution with only separate inversions.

I now adopt the described workflow for the MOSJI. So, I used the described procedure to build a reference model and the inhomogeneous model weighting function for G_z. Both G_z and G_{zzz} model (Fig. 2.7c-d) are instead able to describe the shallower and the deep-seated sources. I can see a rather accurate positioning of the cavities with a proper density contrast. The model resulting from G_z (Fig. 2.7c) recovers slightly better the deeper source with an improved overall positioning and extension of the cavity when compared to that produced by G_{zzz}. Once again, this reflects the different sensitivities brought by the dataset. I noticed that the same considerations done before for the data misfit are valid also in this case.

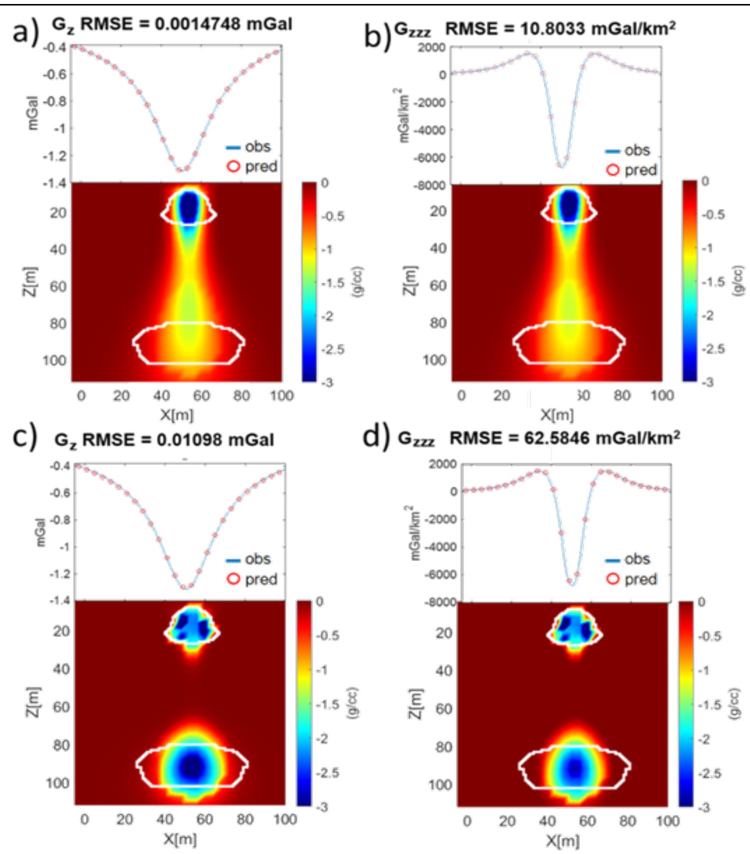

Figure 2.7: model resulting from a) separate inversion of G_z; b) separate inversion of G_{zzz}; c) MOSJI on G_z; d) MOSJI on of G_{zzz} .

The analysis of the cross-gradient values (Fig. 2.8a-b) confirms the results obtained in the synthetic test at basin scale. The most interesting result is that also in this case is to obtain a linearization of the physical parameters in the cross-plot of the jointly inverted models (Fig. 2.8d) with respect to that of separate inversions (Fig. 2.8c). In this case, the divergent behaviour in the tail of the cluster is lost compared to that observed in the previous test (Fig. 2.5d). This is due to the fact that in this model both the sources have the same density contrast.

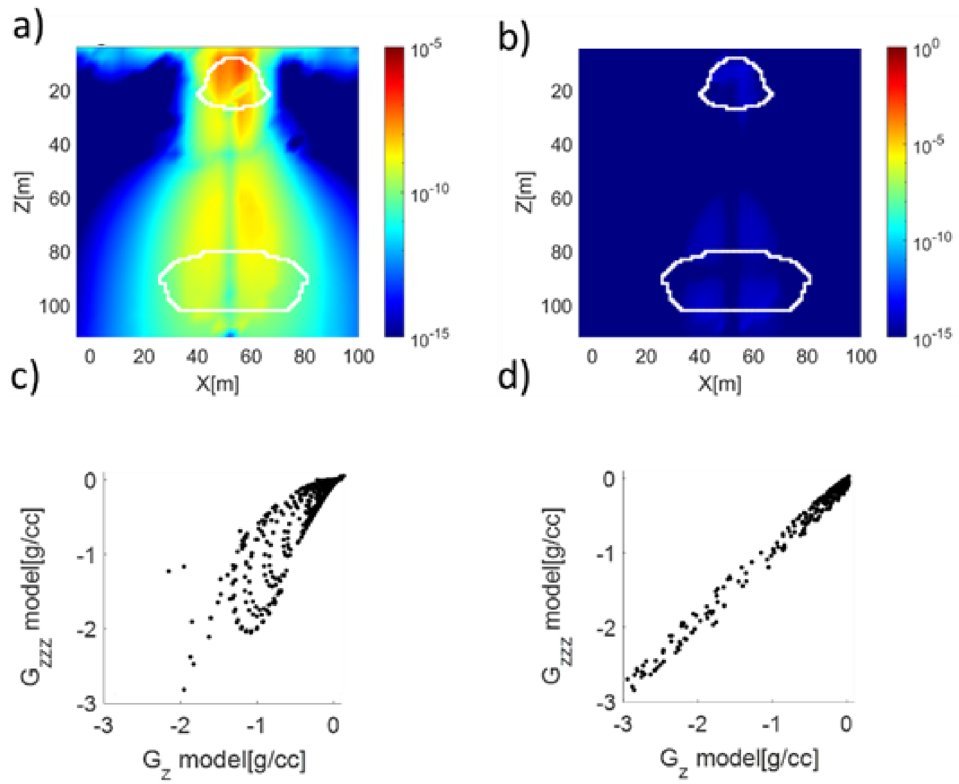

Figure 2.8: a) Magnitude of cross-gradients value of separate inversions; b) scatter plot of density models of separate inversions; from: c) Magnitude of cross-gradients value of MOSJI; d) scatter plot of density models of MOSJI.

2.4 Real case: Gruta de Las Maravillas

I now apply my method to a real case for cavity detection in Southern Spain. I investigated the Gruta de las Maravillas in Aracena. It was previously studied Martínez-Moreno et al. (2014) and interpreted with forward modelling. The cave lies within marbles and its genesis is due to the dissolution of these rocks. It consists of three different levels with a water table that is present at 650 m a.s.l (Martínez-Moreno et al., 2016). I performed my joint inversion on the central part of the Line 4 (Martínez-Moreno et al., 2014), that I resampled at 2m (Fig. 2.9a). I computed the G_{zzz} (Fig. 2.9b) as already discussed. Further information on the gravity data could be found in the afore mentioned works. The zero-level of my model coincides with the maximum of the topography of the line. The model consists of 50x35 cubic cells with a side dimension of 2m. In this case, I used a reference model with the solution of an unconstrained preliminary inversion of G_{zzz}, which was cut at a threshold of -2.5 g/cc. This is justified as a known density contrast of void in marbles.

Results suggest the presence of three shallow cavities with a density contrast of around 2.7 g/cc, that well represents a typical density contrast of air-filled cavities within marbles (Fig. 2.9c-d). These three sources have been also retrieved in the modelling of Martínez-Moreno et al. (2014). The horizontal position is consistent between the forward model and my interpretation, locating the shallow-seated group of cavities at a distance from 180 m to 250 m on the original line. The central cavity of the group is slightly deeper in my modelling than in the forward model (Martínez-Moreno et al., 2014), which locates this cavity at about 20 meters depth.

Following the proposed approach, once again I am able to model the deepest sources (Fig. 2.9c-d), thanks to their different wavelength-content. I found a deeper cavity with its center at about 80 m depth and with a 50 m extension. The forward modelling (Martínez-Moreno et al., 2014) proposed an elongated horizontal source between 50- and 75-meters depth. The positioning is slightly different in the two interpretations, but their ranges are comparable.

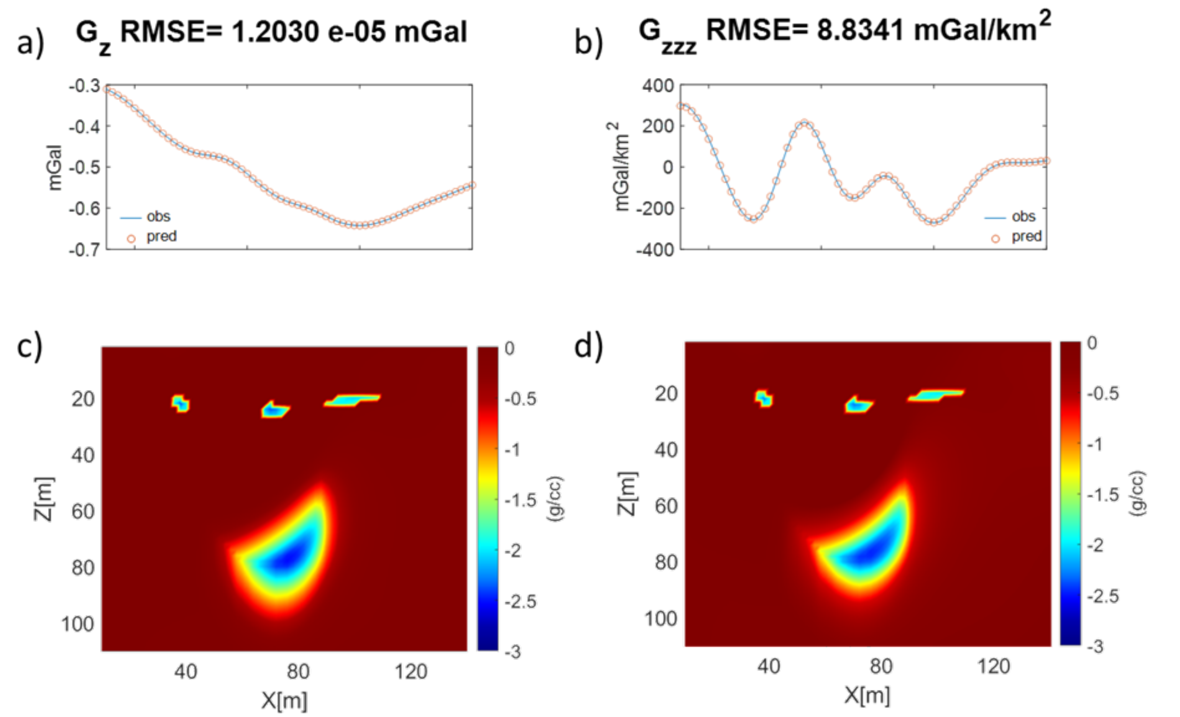

Figure 2.9: a) observed and predicted Gz; b) observed and predicted Gzzz; c) model resulting from joint inversion of Gz; d) model resulting from joint inversion of Gzzz.

In addition, forward model (Martínez-Moreno et al., 2014) suggested an elongated appendix on the upper right corner of this cavity. I have confirmation of this possible features in my modelling. Martínez-Moreno et al. (2014) provide also resistivity, induced polarization and seismic modelling on the same profile. Seismic data modelling clearly shows the presence of the two lateral sallower cavities as low velocity zones with a low number of rays respectively in the velocity model and ray tracing coverage model. The central cavity is not clearly interpretable, but its presence is confirmed by gravity modelling presented both here and in the aforementioned work (Martínez-Moreno et al., 2014). Resistivity and Induced Polarization model are more informative on the elongated appendix of the deeper sources which is recovered in my results and suggested by the forward modelling (Martínez-Moreno et al., 2014).

Analysis of the cross-gradient (Fig. 2.10a) is comparable in magnitude and distribution with those obtained in synthetic tests, with the highest values located on the edges of sources. In the end, I obtain a linearization in the cross-plot of physical parameters (Fig. 2.10b).

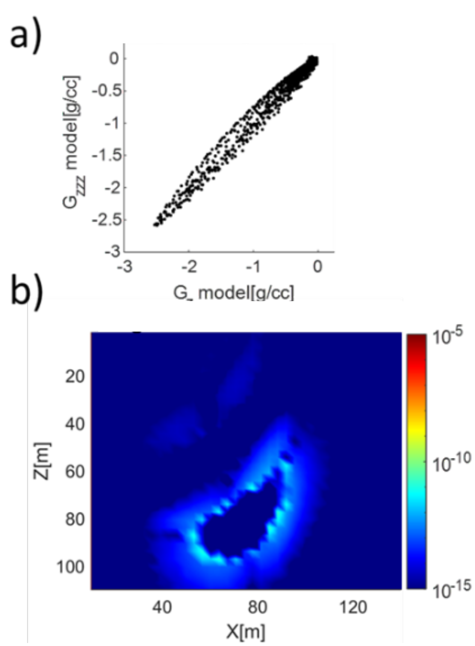

Figure 2.10: a) scatter plot of the physical parameters; b) magnitude of cross-gradients.

3 Seismo-gravity joint inversion

4 Deep-learning gravity inversion based on building blocks learning

This chapter is from:

- *Deep-learning gravity inversion based on building blocks learning; Messina C., Bianco L., Fedi M.; 2024; Under Review at Geophysics.*

Supervised ML methods create a system that learns or improves performance based on the data they use. This is completely different from inverse modelling involving physical knowledge of the problem. It is possible to distinguish between two main types of ML algorithms:

- Unsupervised Machine Learning, where algorithms find patterns in their own data, without guidance.
- Supervised Machine Learning, in which the network tries to do prediction starting from a pair of features-labels.

Supervised Machine Learning is not explicitly based on physical equations but extracts the relationship between data and sources thanks to a training on large ensembles of samples (Shi et al., 2023). ML inversion optimizes a parameterized function, often implemented using neural networks, to predict underground structures based on observed data.

Among the other authors that explored ML methods for potential fields, I recall some works that contributed to the development of the topics. Al-Garni (2015) adopted a Modular Neural Network (MNN) for the interpretation of magnetic anomalies caused by a dike. He estimated the top depth, the half width and the dip of the dike, and also the inclination and the intensity of magnetization. Bernstein et al. (2022) adopted a strategy based on CNN for the recognition of complex magnetic signatures caused by metallic pipelines. They created a 2D CNN to distinguish the presence of pipelines in synthetic gridded magnetic data. The labels of CNN will be equal to 1 if the features are identified as pipelines and to 0 elsewhere. Cutaneo et al. (2023) used an unsupervised Machine Learning technique, called

Unsupervised Boundary Analysis (UBA), to identify without a priori information the sources edges of potential fields. They used Self-Organized Maps and *k*-means algorithms. In this sense, they aimed to reduce the dependency of the interpretation on the geometry of the training models.

The increasing use of supervised ML algorithms in applied geophysics has been accompanied with enthusiasm in its ability to extract relationships between data and models, which is referred to as "data-driven" nature. This has been always opposed to inversion algorithms which by definition are "physics-driven" method and could be seen as "model-driven" method when strong a-priori information are introduced. In applied geophysics the lack of enough real data and true model poses a severe limitation on the data-driven behavior of ML algorithms. To this end, the common approach is to build synthetic training datasets with different strategies (e.g., random walk algorithms).

Authors approached this issue in different ways. Huang et al. (2021) applied a CNN to the 3D inversion of gravity data. They generated as much as 20000 training models, obtained from a random walk algorithm. Deng et al. (2022) adopted CNN to predict physical parameters from 2D images of the magnetic gradient tensor. They extracted information of geometry, depth and magnetization such as inclination and declination obtaining a 3D model. Vitale et al. (2023) used the Bishop synthetic model to train a feed-forward network to reconstruct the depth of the basement. The dataset of gravity anomalies was organized associating the basement depths to their gravity data within a moving window, so resulting into a dataset of about 30000 examples. More recently, Bianco et al. (2023) shaded light on the need to train a CNN with a dataset consisting in gravity anomalies fault like sources.

In this sense, one should look at these ML algorithms as data- and model-driven method, since the assumptions made to build the training set constitute, in principle, an a-priori information. However, this approach clashes with the intrinsic nonuniqueness of the potential fields. To this end, I studied the possibility to simplify the gravimetric anomalies and reduce the training set to the source-anomaly pairs that represent the "building blocks" of the method. In this way, I want to circumvent the problem of facing nonuniqueness by constructing a complex training set and model gravimetric anomalies by the sum of simple sources.

ML algorithm

Supervised Machine Learning is not explicitly based on physical equations but extracts the relationship between data and sources thanks to a training on large ensembles of samples (Shi et al., 2023). ML inversion optimizes a parameterized function, often implemented using neural networks, to predict underground structures based on observed data (Zhang et al., 2022).

In the framework of the Supervised ML methods, I will use in this work a Convolutional Neural Network (CNN). The relationship between data and model may be expressed as:

$$\mathbf{m}=N(\mathbf{d};\,\boldsymbol{\theta}) \tag{4.1}$$

where $\boldsymbol{\theta}$ is a set of parameters to be learned and N the mapping function. $\mathbf{d}$ represents the observation data input, here called features, to the neural network. Finally, $\mathbf{m}$ represents the model output, here called labels, as predicted by the neural network. The misfit between predicted and real labels is used as a loss function to optimize the neural network parameters. The optimization formula can be expressed as:

$$\varphi = \arg min_{\theta}\ \frac{1}{N}\sum_{i=1}^{N} L(\boldsymbol{m_i}, N\ (\mathbf{d_i};\ \boldsymbol{\theta})) \tag{4.2}$$

where $L\ (\cdot)$ represents the loss function, $\boldsymbol{m_i}$ represents the i^{th} label, and $N\ (\mathbf{d_i};\ \boldsymbol{\theta})$ represents the model output by the neural network.

When the value of the loss function exceeds a specified threshold or the maximum number of iterations is reached, the loss is backpropagated to update the neural network parameters. This process ensures that the model learns from its mistakes and adjusts its internal weights and bias to improve performance. The dataset is characterized by pairs of features-labels:

$$T = \{\mathbf{x}_i, \mathbf{d}_i\}_{i=1}^{M} \quad (4.3)$$

Where **T** is training sample ensemble, $\mathbf{x}_i$ is the feature vector of the i^{th} model; $\mathbf{d}_i$ is the label vector of the i^{th} model; M is the size of the sample. The features $\mathbf{x_i}$ are the inputs to the machine learning algorithm, and in my case, they are the set of the gravimetric anomalies generated by elementary blocks. The latter are the labels of the network. **T** is used during the training phase to guide the learning process.

Building Blocks

I describe a method to reconstruct complex sources through the creation of a generalized dataset composed of the fields of elementary sources, such as faults with varying parameters such as dip, density contrast, thickness and depth to the top. The set formed by these sources is a sort of "building blocks" set which I may utilize to reconstruct a general source. For this reason, the ML method is named 'FaultNet3D'.

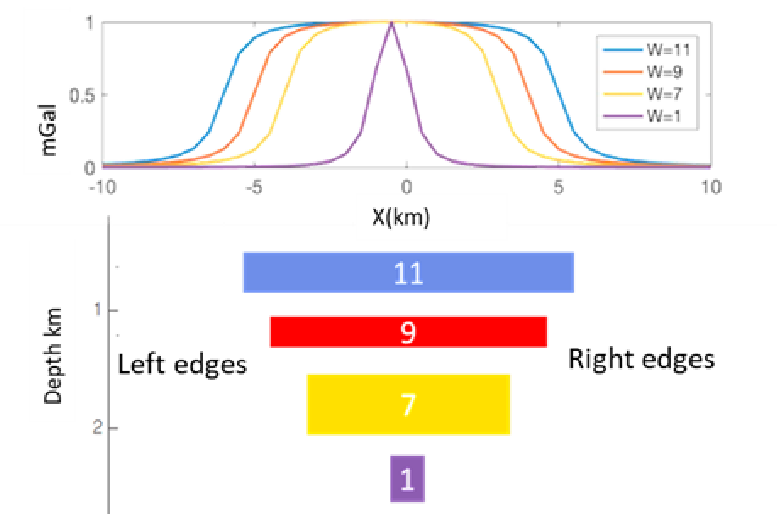

Figure 4.1: Gravity anomalies caused by prismatic sources of different width W.

The procedure is the following: gravimetric anomalies of bodies of different extent are represented in (Fig. 1) by red, blue and yellow profiles. If one examines their own behaviour around the edges of their respective sources (Fig. 2) it is possible to observe how the anomaly takes a characteristic Z-shaped form (right edge) or S-shaped form (left edge). This behaviour is typical of contacts and faults. In other words, a gravimetric anomaly, when analysed along a profile crossing the source, can be seen as composed by the constructive interference of anomalies generated by the edges of the source bodies. When the mutual interference is too strong, as for prisms of limited length, the anomaly takes on its well-known bell shape (purple line in Fig. 1).

In the learning phase the building blocks are characterized by various depth-to-top, thickness, width, dip and density contrasts. The strategy, hence, will consist of: A) interpreting along many 2D profiles the gravity anomaly through my Machine Learning algorithm; B) building a 3D reference model by merging the interpreted 2D models; C) obtaining a final 3D model by data inversion constrained by the reference model.

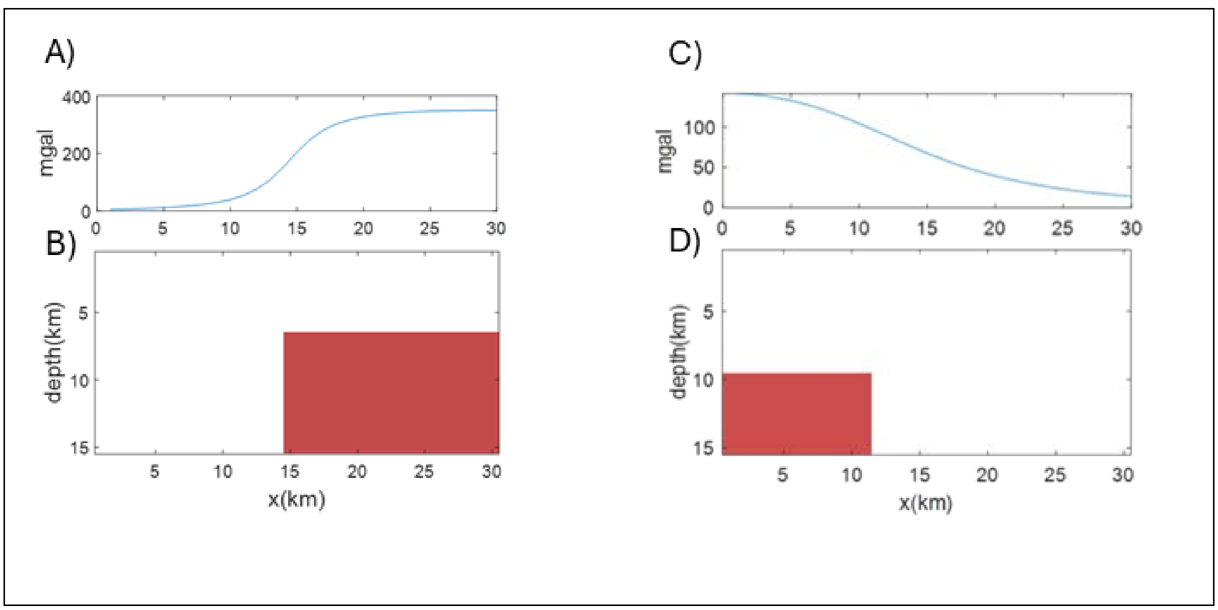

Figure 4.2: Gravity anomalies of contacts with their characteristic Z and S shapes. A) S-shaped anomaly; B) Contact source of the S-shaped anomaly; C) Z-shaped anomaly; D) Contact source of the Z-shaped anomaly.

Network Architecture

The first step is to create a generalized dataset composed by fault-like building blocks and their corresponding gravimetric anomalies. To this end I generated a large set of different types of fault models, by varying their parameters (Table 4.1). Instead than using standard gravity formulas for contacts and faults, I have adopted a different forward modelling method, consisting in generating 2D sections of *M*x*N* prismatic cells to which the density is assigned so as to approximate different types of faults and contacts. The fields of any cell were generated with the formula of Bhattacharyya (1964). Compared to the parametric formulas, this approach better fit the aim of obtaining a final tomographic model of complex sources and gives more flexibility for future developments of the method.

PARAMETERS	RANGE
Density contrast	-1 g/cm^3 to 1 g/cm^3 with 0.1 g/cm^3step
Top depth	1 km to 14 km with 1 km step
Bottom depth	2 km to 15 km with 1 km step
Horizontal extent	1 km to 29 km with 1 km step
Dip	from 10° to ± 90°

Table 4.1: Parameters ranges.

I was able to reproduce in this way up to 221.100 different models. The resulting faults can be classified into the following types: faults with a low dip angle such as thrust type (Fig. 3A), high dip-angle (Fig. 3B) and vertical faults (Fig. 3C) as well as mixed models. After calculating the synthetic gravimetric anomalies for the various models, I constructed the features-labels pairs shown in (Fig. 3). The dataset was randomly divided into three sets:

- Training Set, containing the subset of **T** used by the network for training. This set is the 85% of the total one.
- Validation set which is the subset of **T** that the network uses to validate the training. In this set there are 10% of the total models.
- Testing Set containing a subset of **T** used to test the network. This set contains the 5% of the total models.

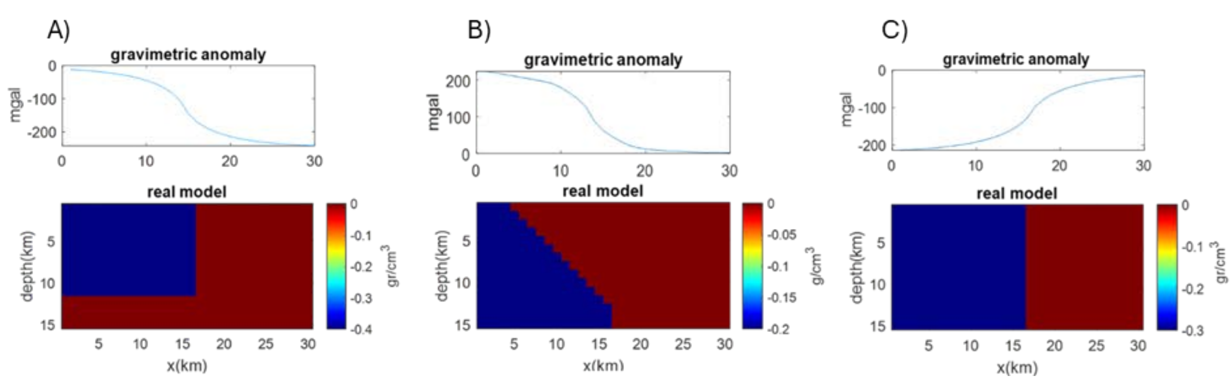

Figure 4.3: Representation of different types of faults containing in the dataset; A) Low dip angle faults; B) High dip-angle faults; C) Vertical Faults.

For the network architecture I was inspired by the work of Wang and Xu (2021). They defined a Siamese structure, called in this way because it uses two twin CNN with the same architecture and sharing of the weights of neurons. In this work, I adopted the architecture of a single branch of the Siamese structure. Moreover, I made the CNN shallower by decreasing the total number of the layers. From a parametric point of view, I used the same values. The choice of such a simple architecture relies on the will of exploring and testing the concept of using the “building blocks” as elementary source to build an enough generalized training set. The network architecture is shown in (Fig. 4.4).

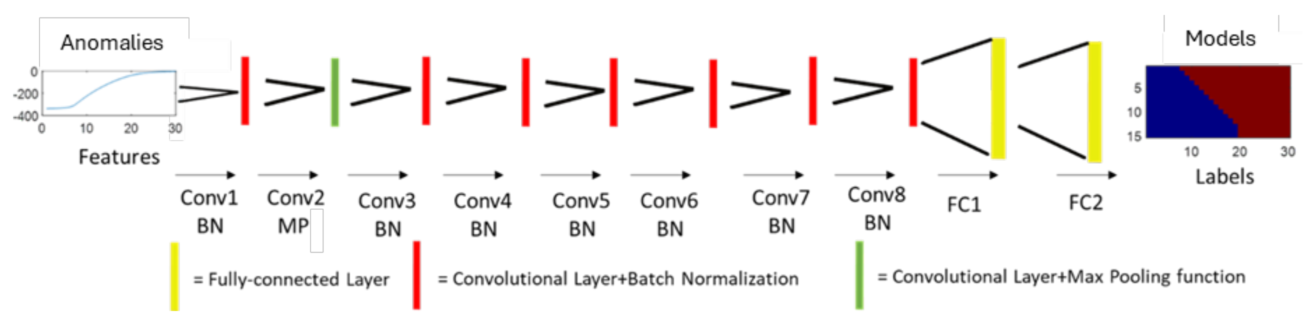

Figure 4.4. Architecture of Convolutional Neural Network (CNN); BN is the function of Batch Normalization; Conv 1-8 are the convolutional layers; MP is Max Pooling function; FC1-2 are the fully connected layers.

The network architecture is characterized by 8 convolutional layers, 1 max pooling (after the second convolutional layer) and 7 batch Normalization functions that are used after the convolutional layers 1, 3, 4, 5, 6, 7, 8. Finally I used 2 fully connected layers and a regression output. Each convolutional layer is followed by a clipped ReLu activation function. The latter allows setting any negative input value to 0 and any value that is above a threshold value, chosen by the operator, to the aforementioned threshold value also called "clipping celling". It allowed to prevent the output value from becoming too large. The negative values will then be retrieved via the BN normalization function.

To build this architecture I used the MATLAB Deep Network Design toolbox and The Adam algorithm (Adaptive Moment Estimation) as optimizer, a stochastic method based on the descent gradient. With this architecture, I trained the network and tested the validation of the training. I tested the performance of the training with the model contained in the Test Set, selected in a random way. (Figure 5.5) shows one of these tests. My network demonstrated to be able to accurately interpretate the density contrast between the sources and the background, the geometry and the position of the bodies.

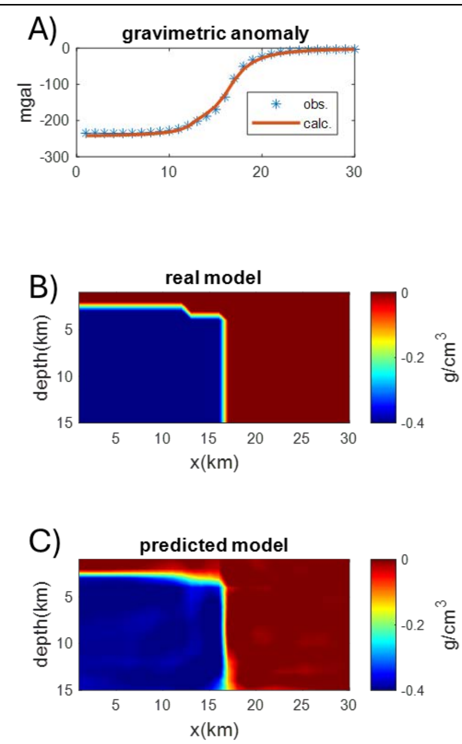

Figure 4.5. Testing model. A) Misfit between observed data and calculated data. B) Real model C) Predicted model from the neural network.

Synthetic modelling

As a first test, I applied the network to a synthetic case. I created a pyramid-like source which, for geometries, density contrasts and extension can be seen as a simplification of a salt dome (Chen et al., 2023). The density contrast between the source and the background is -0.3 g/cm^3. The body is shown with the vertical section at y=21 km (Figure 5.6a) and different depth slices (Figure 5.6b). I then computed its gravity anomaly, from which I extracted 8 radial profiles, equally spaced 22.5°. Following my approach, each profile was divided into two parts (AO and OA'), corresponding to Z-shaped and S-shaped anomalies, respectively. The ML interpreted models obtained along the profiles are shown in figure (4.7), in which I can observe again that the network reliably predicts the density contrast and also the shape and the position of the body.

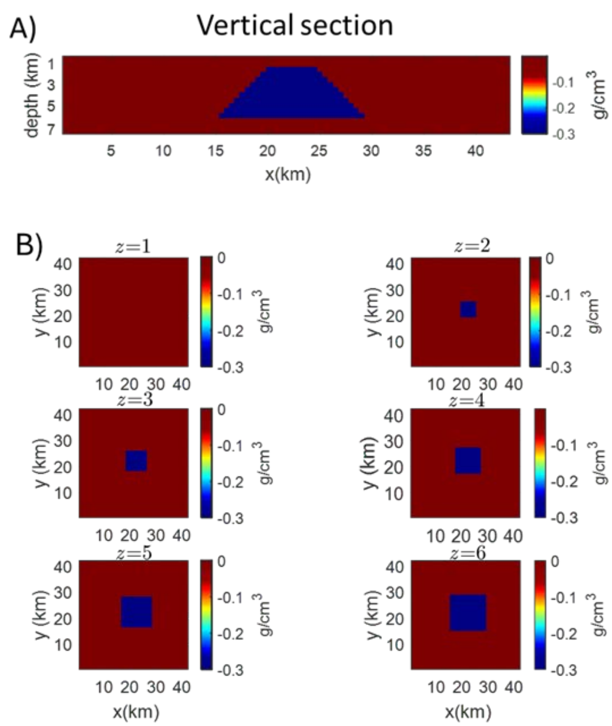

Figure 4.6: A) Vertical section of synthetic model; B) Depth slices of synthetic model respectively at different depths.

I then computed its gravity anomaly, from which I extracted 8 radial profiles, equally spaced 22.5°. Following my approach, each profile was divided into two parts (AO and OA'), corresponding to Z-shaped and S-shaped anomalies, respectively. The ML interpreted models obtained along the profiles are shown in figure (4.7), in which it is possible to observe again that the network reliably predicts the density contrast and also the shape and the position of the body.

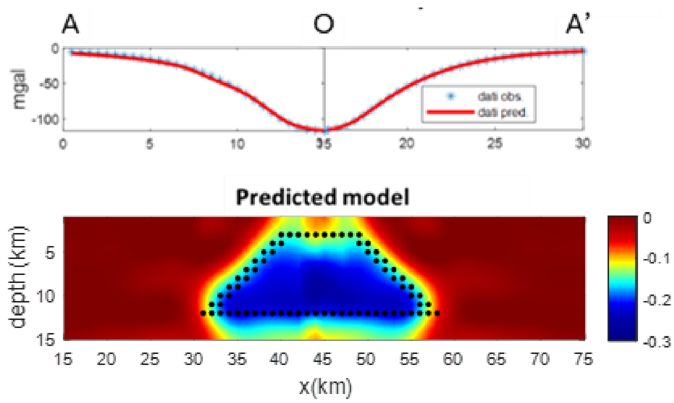

Figure 4.7: FaultNet3D interpretation of the profile A-O-A', the black points represent the position of the synthetic source.

After obtaining these sections, I performed a 3D interpolation to create a 3D reference model to be used in a standard 3D inversion algorithm (see chapter I). For what it concerns the β exponent (Eq. 1.11), it has been chosen according to the strategy of Cella and Fedi (2012). They suggested that the model depth weighting exponent β is effectively depending on the source model rather than to the power-law decay of a single cell, so that $\beta=N$. N may be estimated by specific techniques, or it may be assumed as a priori information on the type of source.

I compared the results obtained from the inversion with the reference model derived from the FaultNet3D algorithm, with those obtained with the inversion unconstrained from the reference model.

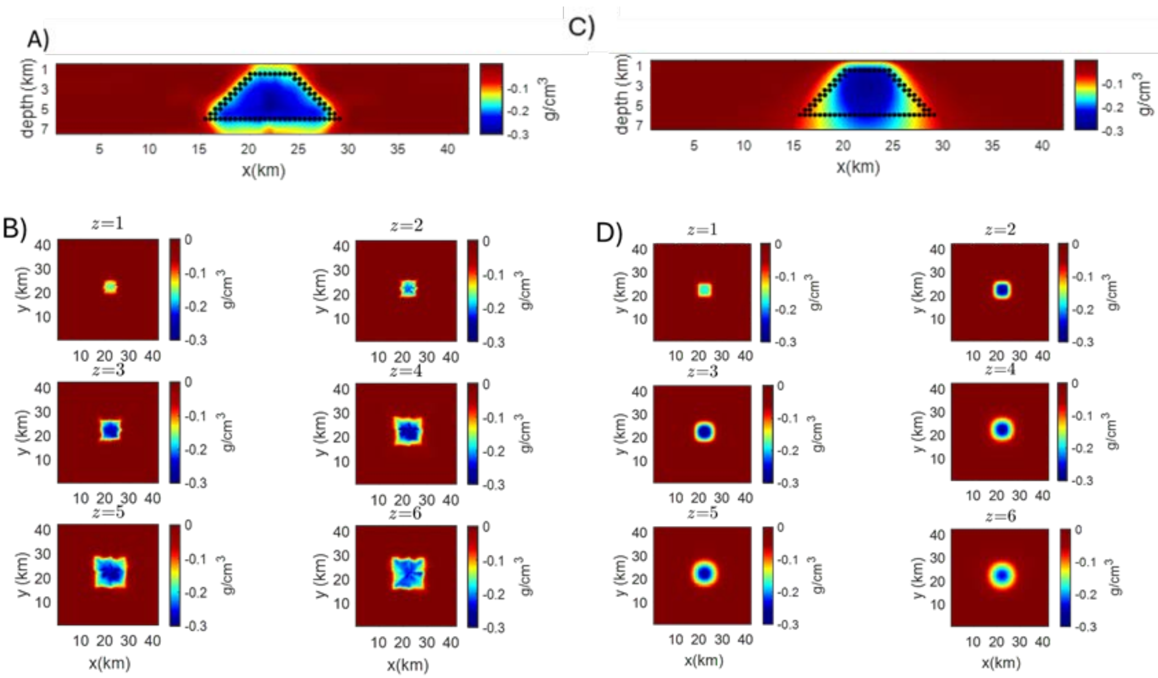

Figure 4.8: Comparison between inversion constrained with the ML reference model A) sections; B) depth slices; and unconstrained inversion C) sections; D) depth slices. Black dots in the vertical sections indicates the source.

From the comparison among these images, I observe that the inversion with Machine Learning reference model is able to reproduce fairly well the position, density contrast and shape of the source, improving the results obtained by the FaultNet3D interpretation. On the other hand, Figure (4.8B) shows that the unconstrained inversion does not reproduce well either the shape or the position of the source. In particular, the bottom closes at a much greater depth than the real one.

Real case: Caltanissetta Basin, Italy

As a real case, I choose that of the Caltanissetta basin (Sicily, Italy) which is a deep and wide sedimentary basin. The gravity map was digitized with a 2 km sampling rate. The Bouguer plate density contrast was 2.67 g/cm^3. Data were upward continued to a common altitude of 3.2 km (Milano et al., 2020).

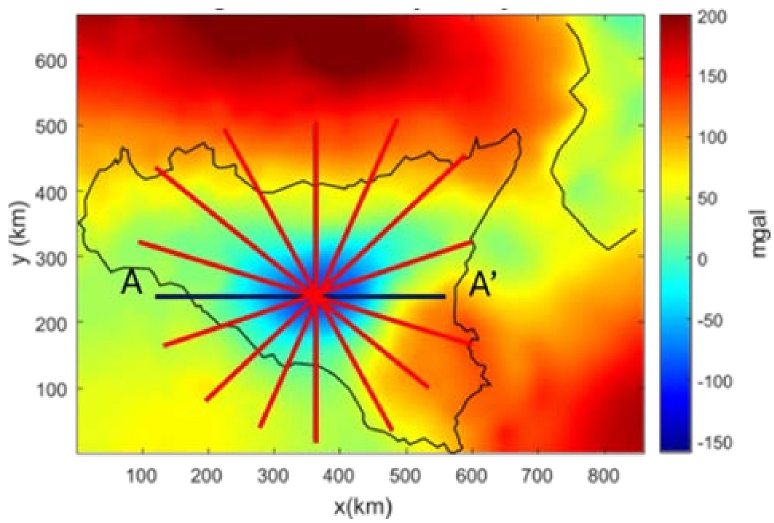

Figure 4.9: Gravimetric anomaly of Sicily. In red the profiles interpreted.

The Caltanissetta Basin corresponds to the main depozone of the Sicilian-Maghrebian foreland basin system. It is located between the northern Sicilian Mountains (Sicani and Madonie Mountains) and the southern Sicilian Fold and Thrust Belt (SFTB). This basin was formed during the opening of the southern Tyrrhenian Sea in the late Miocene and during the compression and shortening of the Sicilian-Maghrebian chain. Over time, the accretionary front has shifted southward and south-eastward, advancing approximately 50 km between the early Pliocene and early Pleistocene (Catalano et al., 2000; Tzevahirtzian et al., 2023). Its complex morpho-structural framework results from the progressive accretion of thrust sheets and duplex formation from paleogeographic domains of the oceanic one of Neo-tethys and the African continental paleo-margin. During Neogene times, a series of wedge-top basins were formed, characterized by several depocenters separated by intrabasinal highs and related to the Messinian active thrusting synclines (Butler et al., 1995). The basin is filled with Pliocene-Pleistocene marine deposits, such as deep-sea carbonates, which overlap each other and finally slide into the basin (Scandone et al., 1975). The stratigraphy, from bottom to top, is the following: Iblean units and Trapanese units which are composed by Meso-Cenozoic shallow water to pelagic deposits; Sicans units consists in Permian-Cenozoic deep-water deposits; Numidian Flysch units which incorporate part of Sicilide units; On the top there are evaporites deposits of the Messinian and Pleistocene foreland deposits. The Messinian sedimentary deposition in the Caltanissetta sub-basin has historically been regarded as the comprehensive geological record of the Sicilian crisis. Its tripartite structure makes it an excellent counterpart to the seismic 'trilogy' observed in the deep Mediterranean basins (Lofi et al., 2011; Roveri et al., 2014).

Many gravity, magnetic and seismic studies have been conducted in the area. Among them, Milano et al. (2020) used gravimetric and magnetic data to reconstruct the depths to the crystalline basement, to the Moho and to the top of the carbonate platform. Accordingly, the basin bottom is deep down to 16 km depth below seas level, with a -0.2 g/cm^3 mean density contrast between the clastic infilling and surrounding rocks. Similarly, Sgroi et al. (2012) proposed a seismo-tectonic interpretation of the basin with a 16 km estimated maximum depth. Finally, a seismic profile was acquired through the Caltanissetta basin, processed and interpreted by Catalano et al. (2013). In this work they interpreted and divided the basin in different units. According to them, the Crystalline basement is at a 24 km depth.

I used the same workflow applied to the synthetic case. Thus, I extracted 8 radial profiles from the map (Figure 4.9), dividing each of them into two sub-profiles. The ML interpreted profiles were then interpolated to obtain a 3D reference model. The Figure (4.10 A) show the results of constrained inversion along the profile A-A’, in which it is possible to observe that the equivalent density contrast between the sediments that fill the basin, and the background is -0.2 g/cm^3. In Figure 10B, the depth slices show that the basin ends at around 16 km Note that, the results of modelled basin are comparable to those present in literature (Sgroi et al., 2012; Milano et al., 2020) who estimated the depth of the basin around 16 km. In addition, for geometries and depth, I can associate it to the top of autochthonous of Iblean Unit present in the interpretation of (Catalano et al., 2013). On the contrary, figure 10C, illustrates that the unconstrained inversion leads to a too smooth representation of the basin, with an equivalent density contrast of around -0.1 g/cm^3. Note also that the basin extends too deep, down to around 24 km (Figure 10 D), which is much greater than the depth estimated from literature by the previous work (Sgroi et al., 2012; Catalano et al., 2013; Milano et al., 2020).

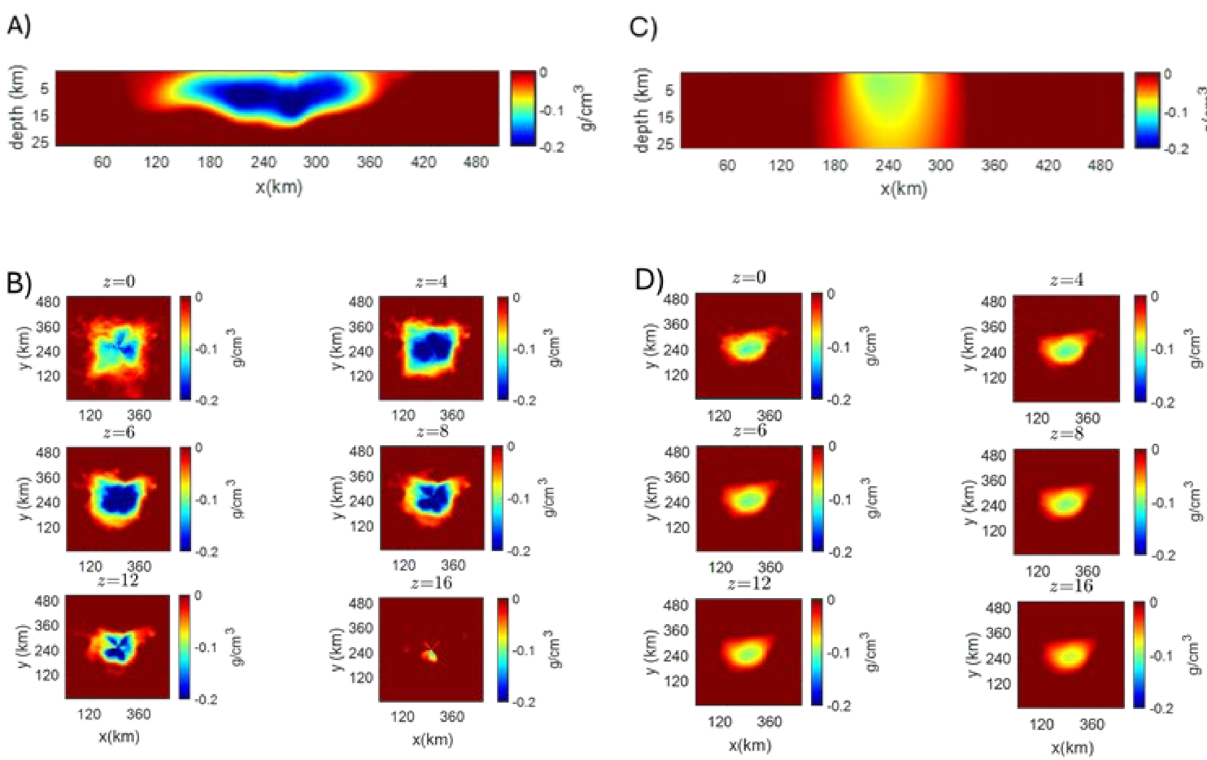

Figure 4.10: Comparison between the constrained inversion with a reference model (A-B) and unconstrained inversion without reference model (C-D).

CONCLUSIONS

Starting from the scenario of Skeels (1947) evoking an absolute ambiguity for potential fields, I proposed new approaches to unveil what is really ambiguous and what may instead be determined in the source domain.

To accomplish this goal, I studied the advantages given by using different datasets in the interpretation of potential fields. The possibility of integrating more dataset means that more information is brought into the interpretation processes, so to allow a reduction of ambiguity. In this sense, I used the gravity field at different altitudes and at different orders of differentiation, in a multiscale approach, and the integration of potential fields with other geophysical datasets.

In the first approach, I analyzed the behavior of the fields generated by a step and a flexure at different altitudes and different order of differentiation. I was able to study the properties of these fields and extract self-constraints from the field themselves. This strategy led to the definition of relative ambiguity, meaning that the ambiguity regards not all the harmonic region but only a part of it, called *region of ambiguity*. From these findings, I introduced a new multiscale method based on the DEXP transform of the field, called Inhomogeneous DEXP, where the scaling exponent is not necessarily constant at different positions, but varies with the homogeneity degree of the field. I obtained models that demonstrated improvements in the imaging of the complex bodies' geometries which are brought by the adoption of an inhomogeneous exponent.

Regarding the joint inversion framework, I used first gravity data with no other different geophysical data (such as DC resistivity, magnetic or seismic), but with the high-order vertical derivatives of the Newtonian gravity potential. My idea was that the different wavenumber-content of these dataset alongside with the self-constraints extracted from the field themselves (e.g., an inhomogeneous model depth-weighting function) could reduce the inherent ambiguity. The integration of multi-order dataset was achieved via the so-called sequential strategy with the cross-gradient constraint. This feature lets us to separately invert two datasets and iteratively enforce their structural similarity without incurring in the need of a unique objective function to be minimized. Using this approach, I was able to successfully model different scenarios in which vertically-stacked sources represent a tricky challenge for interpretation (e.g., salt domain and multi-level karst system). The goodness of the result were demonstrated by the minimization of the cross-gradient and looking at the linearity of the distribution among the models' properties.

I used further this sequential strategy formulating a workflow for a joint inversion of gravity data and seismic-derived/geological models. In this sense, I aimed at generating density models inverting gravity and gravity gradient data based on the structural information derived from s seismic model without the need of any physical-parameters conversions. The main advantage of this approach is that we can avoid seismic data inversion and look at the final density model to obtain precious information on both the main bodies (for instance, the salt dome) and the background (for instance, the layer densities around the salt body). The workflow enforces the structural similarity between the density model and the seismic model but still fitting the gravity measurements. In this way, we are able to detect those portions of the density model in which artifacts are present (e.g., gravimetric pushdowns) and thus improve the final density model. The final model could be useful to confirm seismic modelling or to provide useful information for a subsequent update of the models, in a cyclic procedure involving seismic and potential fields with the common aim of reducing uncertainty and ambiguity in subsurface interpretation.

For clarity, although I have developed and coded these algorithms for 3D joint inversions now I was able to test the methods only on 2D cases, due to lack of a sufficient computational power. However, small-scale synthetic tests proved the actual efficiency of the inversion codes even for 3D cases. For this reason, the methods require coding adaptations to run on cluster and/or cloud computing so unlocking their full capacity.

Moreover, the algorithms could be further improved by introducing more refined mathematical tools to reduce the computational loading required for large-scale 3D inversions.

Finally, I moved the focus of my research on ML algorithms. In particular, I proposed the strategy of training a ML algorithm with a set of simple sources, which I called building blocks, and their own gravity anomalies. My assumption was that complex geometries could be analysed by a CNN as the ensemble of gravity anomalies generated by the edges. Hence, the strong constraint of looking only at the edges of the sources represents a practical way of facing the non-uniqueness of the solutions.

However, this strategy requires the interpretation of 2D gravity data to preserve the validity of the assumption that the edges of a given source could be seen as faults/contacts. For this reason, I proposed to merge 2D interpretations into a reference model to constrain a 3D gravity inversion. This could be seen as extracting a “self-constraint" from the field itself, thanks to the strong information related to the assumed building-blocks. Thus, the method (called FaultNet3D) was proved to yield a useful and reliable strategy to obtain a constrained model even when external a-priori information is not available, or it is rather not useful.

The possibilities of further developments are represented by improving the width of the ranges adopted to build the training models. In addition, the approach could be used to train an ad-hoc deeper network to improve the performances or a Siamese network to include higher-order of vertical derivation of the gravity field or magnetic data. This last possibility was not explored as I wanted to avoid any influence brought by a deep network and look only at the behaviour of the building blocks training set.

The new concept of "*region of ambiguity*" and the new tools introduced: Inhomogeneous DEXP, multi-order sequential joint inversion, seismo-gravity joint inversion and Fault3DNet represent very promising tools in the challenge of reducing ambiguity in potential fields modelling. The results demonstrated that an accurate study of the data together with a proper multiscale approach and a wise usage of constraints and AI algorithms could efficiently support applied geophysicists in different stage of the exploration.

Finally, I want to underline that all the studied scenarios represent important cases targeted by the United Nation Sustainable Development Goals. In fact, I showed the case of an abandoned mine (Udden Mine, Sweden), karst cavities (Gruta de Las Meravillas, Spain), salt dome (Mors, Denmark) and a sedimentary basin (Caltanissetta, Sicily) which are studied and explored for environmental, energy transition and hazard management purposes.

APPENDIX

A1- Scaling function

This part is extracted from: Vitale and Fedi (2020).

Scaling functions are important to understand the homogeneous properties of potential fields. In the following demonstrations, the cartesian coordinate system is assumed with the z-axis negative downward.

The gravity field $f(\mathbf{r})$ due to a homogeneous sphere at $\mathbf{r}_0(x_0, y_0, z_0)$ with density M=1 and normalized by the gravity constant k, can be expressed as:

$$f(\mathbf{r}) = \frac{(z-z_0)}{\|\mathbf{r}-\mathbf{r_0}\|_2^2} \quad \text{(A1.1)}$$

If the source is at r_0 (0,0, z_0) and the field is measured at $x=x_0$, $y=y_0$ this results in:

$$f(z) = \frac{1}{(z-z_0)^2} \quad \text{(A1.2)}$$

The scaling function can be defined as the derivative of the logarithm of the field f with respect to log(z):

$$\tau\,(z) = \frac{\partial log[f(z)]}{\partial log(z)} \quad \text{(A1.3)}$$

For the above-mentioned example of the gravity field, the scaling function τ is:

$$\tau\,(z) = -\frac{2z}{z-z_0} \qquad \text{(A1.4)}$$

The scaling function has the important property of not being dependent on the source property, such as density or magnetization intensity. Taking into account a q^{th} order of derivation for the field *f*, it is possible to express the scaling function as:

$$\tau_{\,q}(z) = \frac{\partial log[f(z)]}{\partial log(z)} = -\frac{(k+2)z}{z-z_0} \qquad \text{(A1.5)}$$

From the equation (A1.5) it is clear that $\tau(z)$ is singular at $z=z_0$ in the source region, but at $z=-z_0$ it results in $\tau(z)$ = -1, and it follows that:

$$\left.\frac{\partial\{log[f(z)]+log(z)\}}{\partial z}\right|_{z=-z_0} = \left.\frac{\partial zf}{\partial z}\right|_{z=-z_0} = 0 \qquad \text{(A1.6)}$$

From equation (A1.6) it is easy to understand that the function *zf* has a maximum at $z=-z_0$. This means that, scaling the gravity field with a power law of the altitude *z* and exponent equal to 1, results in a scaled gravity field, *Wg*:

$$W_g = fz \qquad \text{(A1.7)}$$

It is possible to generalize the scaling function formula to any k^{th} order vertical derivative of the field f_k, and to any kind of homogeneous source; in fact, starting from the k^{th} order derivative of the gravity field, of homogeneity degree *n:*

$$f_k\,(x = x_0,\; y = y_0\,,\; z) = \frac{1}{(z-z_0)^2} \qquad \text{(A1.8)}$$

Where $N=-n$:

$$\tau_{\,k}(z) = \frac{\partial log[f_k\,(z)]}{\partial log(z)} = -\frac{(k+N)z}{z-z_0} \qquad \text{(A1.9)}$$

At z=-z_0:

$$\tau_k(-z_0) = -\frac{(k+N)}{2} \tag{A1.10}$$

Hence, the general scaled function, W_k, which is called DEXP transformation, has an extreme point at the source position x=x_0, y=y_0 and z=-z_0 and it can be expressed as:

$$W_k = f_k z^{\frac{k+N}{2}} \tag{A1.11}$$

Obviously real sources generate a field that cannot be explained by something like a simple pole source, unless the field is measured at a great distance. So, real sources are defined as source distributions within finite volumes with arbitrary shapes. But, in some cases, the source complexity can be simplified to semi-infinite volume-less shapes. For example, pipes, ridges, valleys, volcanic necks can be seen as infinite cylinders. These simple shape bodies are generally defined as one-point sources, meaning that of just the coordinates one singular point are sufficient to define them (e.g., center or the edge).

Assuming an ideal source, it is easy to write the most general form of the scaling function t in scalar notation for data at any position **r** in the source-free region, and for the source at any position ***r*** in the source region:

$$\tau_k(\mathbf{r},\boldsymbol{\rho}) = \frac{\partial \log f_k}{\partial \log(x-\xi)} + \frac{\partial \log f_k}{\partial \log(y-\eta)} + \frac{\partial \log f_k}{\partial \log(z-\zeta)}$$

(A1.12)

$$\tau_k(\mathbf{r},\boldsymbol{\rho}) = \frac{1}{f_k}\frac{\partial f_k}{\partial x}(x-\xi) + \frac{1}{f_k}\frac{\partial f_k}{\partial y}(y-\eta) + \frac{1}{f_k}\frac{\partial f_k}{\partial z}(z-\zeta)$$

Equation (1.27) could be written in a different form, as:

$$\tau_k(\mathbf{r},\boldsymbol{\rho}) = \nabla \log(f_k)\cdot\mathbf{r} - \frac{\partial \log f_k}{\partial x}\xi - \frac{\partial \log f_k}{\partial y}\eta - \frac{\partial \log f_k}{\partial z}\zeta =$$

$$= a - b\xi - c\eta - d \tag{A1.13}$$

Where: $a = \nabla \log(f_k) \cdot \mathbf{r}$, $b = \frac{\partial \log f_k}{\partial x}$, $c = \frac{\partial \log f_k}{\partial y}$, $d = \frac{\partial \log f_k}{\partial z}$

Now, the differential scaling function (Fedi and Florio, 2009) can be defined as the gradient **D** of the scaling function τ_k:

$$\mathbf{D} = \nabla \tau_k \tag{A1.14}$$

with components:

$$D_x = \frac{\partial \tau}{\partial x} = \frac{\partial a}{\partial x} - \frac{\partial b}{\partial x}\xi - \frac{\partial c}{\partial x}\eta - \frac{\partial d}{\partial x}\zeta$$

$$D_y = \frac{\partial \tau}{\partial y} = \frac{\partial a}{\partial y} - \frac{\partial b}{\partial y}\xi - \frac{\partial c}{\partial y}\eta - \frac{\partial d}{\partial y}\zeta \tag{A1.15}$$

$$D_z = \frac{\partial \tau}{\partial z} = \frac{\partial a}{\partial z} - \frac{\partial b}{\partial z}\xi - \frac{\partial c}{\partial z}\eta - \frac{\partial d}{\partial z}\zeta$$

Or in matrix notation:

$$\mathbf{D} = \alpha + \Gamma \boldsymbol{\rho} \tag{A1.16}$$

Where: $\alpha = \nabla a$,

$$\Gamma = \begin{bmatrix} \frac{\partial b}{\partial x} & \frac{\partial c}{\partial x} & \frac{\partial d}{\partial x} \\ \frac{\partial b}{\partial y} & \frac{\partial c}{\partial y} & \frac{\partial d}{\partial y} \\ \frac{\partial d}{\partial z} & \frac{\partial d}{\partial z} & \frac{\partial d}{\partial z} \end{bmatrix} \tag{A1.17}$$

Because for homogeneous fields the Euler equation holds, at **r**=**r***(ξ^*, η^*, ζ^*) it results in:

$$\tau_k(\mathbf{r}, \boldsymbol{\rho}^*) = -n \tag{A1.18}$$

It will be:

$$D_k(\mathbf{r}, \boldsymbol{\rho}^*) = 0 \tag{A1.19}$$

Thus, the unknown source position **r*** may be obtained solving the system in eq. (A1.18). Eq. (A1.19) lets us substitute **r*** to **r** in any equations and so estimate the degree of homogeneity *n*.

Now, considering a multi-homogeneity source model, any field from complex source distributions, that is, given by any general source, may be locally approximated at every point **r** by a homogeneous field of degree *n*.

For this reason, it is possible to solve the system deduced from equation (A1.19) at every point **r** of the field domain, to estimate the source parameters ξ^*, η^*, ζ^*. For every position in the space r_i (x_i,y_i,z_i) let us assume $\xi^*=x_i$ and $\eta^*=y_i$. Knowing them and substituting them in equation (A1.18), it is possible to estimate the degree of homogeneity *n* and so *N*, in every *x*, *y*, *z* point in *R*.

REFERENCES

Abbas, M. A., L. Speranza, M. Fedi, B. Garcea, and L. Bianco, 2024, Magnetic data modelling of salt domes in Eastern Mediterranean, offshore Egypt: Acta Geophysica. http://dx.doi.org/10.1007/s11600-024-01284-9.

Al-Garni, M. A., 2015, Interpretation of magnetic anomalies due to dipping dikes using neural network inversion: Arabian Journal of Geosciences, **8**, 8721-8729.

Barbosa, V. C. F., J. B. C. Silva, and W. E. Medeiros, 1999, Stability analysis and improvement of structural index estimation in Euler deconvolution: GEOPHYSICS, **64**, no. 1, 48-60. http://dx.doi.org/10.1190/1.1444529.

Barbosa, V. C. F., J. B. C. Silva, and W. E. Medeiros, 2002, Practical applications of uniqueness theorems in gravimetry: Part II—Pragmatic incorporation of concrete geologic information: GEOPHYSICS, **67**, no. 3, 795-800. http://dx.doi.org/10.1190/1.1484523.

Barton, P. J., 1986, The relationship between seismic velocity and density in the continental crust — a useful constraint?: Geophysical Journal International, **87**, no. 1, 195-208. http://dx.doi.org/10.1111/j.1365-246X.1986.tb04553.x.

Bernstein, B., Y. Li, and R. Hammack, 2022, Automated metallic pipeline detection using magnetic data and convolutional neural networks, Second International Meeting for Applied Geoscience & Energy, 1160-1164.

Bhattacharyya, B. K., 1964, MAGNETIC ANOMALIES DUE TO PRISM - SHAPED BODIES WITH ARBITRARY POLARIZATION: GEOPHYSICS, **29**, no. 4, 517-531. http://dx.doi.org/10.1190/1.1439386.

Bianco, L., C. Messina, and M. Fedi, 2023, Looking for a simplified and generalized training set in ML applications for gravity modelling, Third International Meeting for Applied Geoscience & Energy Expanded Abstracts, 734-737.

Bianco, L., M. Tavakoli, A. Vitale, and M. Fedi, 2024, Multiorder Sequential Joint Inversion of Gravity Data With Inhomogeneous Depth Weighting: From Near Surface to Basin Modeling Applications: IEEE Transactions on Geoscience and Remote Sensing, **62**, 1-11. http://dx.doi.org/10.1109/TGRS.2023.3340037.

Biegert, E. K., M. Talwani, and D. J. Smit, 2001, Gravity Gradients for De-Risking PreStack Depth Migration. http://dx.doi.org/https://doi.org/10.3997/2214-4609-pdb.15.IG-2.

Blakely, R. J., 1996, Potential theory in gravity and magnetic applications: Cambridge university press.

Blakely, R. J., and R. W. Simpson, 1986, Approximating edges of source bodies from magnetic or gravity anomalies: GEOPHYSICS, **51**, no. 7, 1494-1498. http://dx.doi.org/10.1190/1.1442197.

Butler, R. W., W. H. Lickorish, M. Grasso, H. M. Pedley, and L. Ramberti, 1995, Tectonics and sequence stratigraphy in Messinian basins, Sicily: constraints on the initiation and termination of the Mediterranean salinity crisis: Geological Society of America Bulletin, **107**, no. 4, 425-439.

Capriotti, J., and Y. Li, 2014, Gravity and gravity gradient data: Understanding their information content through joint inversions, SEG Technical Program Expanded Abstracts 2014, 1329-1333.

Capriotti, J., and Y. Li, 2022, Joint inversion of gravity and gravity gradient data: A systematic evaluation: GEOPHYSICS, **87**, no. 2, G29-G44. http://dx.doi.org/10.1190/geo2020-0729.1.

Castaldo, R., M. Fedi, and G. Florio, 2014, Multiscale estimation of excess mass from gravity data: Geophysical Journal International, **197**, no. 3, 1387-1398. http://dx.doi.org/10.1093/gji/ggu082.

Catalano, R., A. Franchino, S. Merlini, and A. Sulli, 2000, Central western Sicily structural setting interpreted from seismic reflection profiles: Mem. Soc. Geol. It, **55**, 5-16.

Catalano, R., V. Valenti, C. Albanese, F. Accaino, A. Sulli, U. Tinivella, M. G. Morticelli, C. Zanolla, and M. Giustiniani, 2013, Sicily's fold–thrust belt and slab roll-back: the SI.RI.PRO. seismic crustal transect: Journal of the Geological Society, **170**, no. 3, 451-464. http://dx.doi.org/doi:10.1144/jgs2012-099.

Cella, F., and M. Fedi, 2012, Inversion of potential field data using the structural index as weighting function rate decay: Geophysical Prospecting, **60**, no. 2, 313-336.

Cella, F., M. Fedi, and G. Florio, 2009, Toward a full multiscale approach to interpret potential fields: Geophysical Prospecting, **57**, no. 4, 543-557. http://dx.doi.org/https://doi.org/10.1111/j.1365-2478.2009.00808.x.

Chauhan, M. S., M. Fedi, and M. K. Sen, 2018, Gravity inversion by the Multi-HOmogeneity Depth Estimation method for investigating salt domes and complex sources: Geophysical Prospecting, **66**, no. S1, 175-191. http://dx.doi.org/https://doi.org/10.1111/1365-2478.12603.

Chauhan, M. S., I. Pierri, M. K. Sen, and M. Fedi, 2021, Assessing model uncertainty for the scaling function inversion of potential fields: GEOPHYSICS, **86**, no. 6, G89-G98. http://dx.doi.org/10.1190/geo2020-0557.1.

Chen, B., G. Qi, J. Du, S. Li, and Y. Sun, 2023, 3-D gravity anomaly inversion for imaging salt structures, with application to Vinton Salt Dome, Gulf of Mexico: IEEE Transactions on Geoscience and Remote Sensing.

Coutant, O., M. L. Bernard, F. Beauducel, F. Nicollin, M. P. Bouin, and S. Roussel, 2012, Joint inversion of P-wave velocity and density, application to La Soufrière of Guadeloupe hydrothermal system: Geophysical Journal International, **191**, no. 2, 723-742. http://dx.doi.org/10.1111/j.1365-246X.2012.05644.x.

Cutaneo, C., A. Vitale, and M. Fedi, 2023, Unsupervised boundary analysis of potential field data: A machine learning method: GEOPHYSICS, **88**, no. 3, G57-G65. http://dx.doi.org/10.1190/geo2022-0146.1.

De Stefano, M., F. Golfré Andreasi, S. Re, M. Virgilio, and F. F. Snyder, 2011, Multiple-domain, simultaneous joint inversion of geophysical data with application to subsalt imaging: GEOPHYSICS, **76**, no. 3, R69-R80. http://dx.doi.org/10.1190/1.3554652.

Dejong, H., I. Al-Kindy, and E. Biegert, 2001, Gravity-Gradient Data Integrated in Pre-Stack Depth Migration in the Southern North Sea. http://dx.doi.org/https://doi.org/10.3997/2214-4609-pdb.15.IG-3.

Deng, H., X. Hu, H. Cai, S. Liu, R. Peng, Y. Liu, and B. Han, 2022, 3D inversion of magnetic gradient tensor data based on convolutional neural networks: Minerals, **12**, no. 5, 566.

Fang, Y., J. Wang, X. Meng, S. Zheng, and H. Tang, 2022, An Efficient Cross-Gradient Joint Inversion Algorithm for Gravity and Magnetic Data Using a Sequential Strategy: IEEE Transactions on Geoscience and Remote Sensing, **60**, 1-16. http://dx.doi.org/10.1109/TGRS.2022.3182690.

Fedi, M., 2002, Multiscale derivative analysis: A new tool to enhance detection of gravity source boundaries at various scales: Geophysical Research Letters, **29**, no. 2, 16-11-16-14. http://dx.doi.org/https://doi.org/10.1029/2001GL013866.

Fedi, M., 2007, DEXP: A fast method to determine the depth and the structural index of potential fields sources: GEOPHYSICS, **72**, no. 1, I1-I11. http://dx.doi.org/10.1190/1.2399452.

Fedi, M., 2016a, An unambiguous definition of the structural index, SEG Technical Program Expanded Abstracts 2016, 1537-1541.

Fedi, M., 2016b, Scaling Laws in Geophysics: Application to Potential Fields of Methods Based on the Laws of Self-similarity and Homogeneity, *in* V. P. Dimri, ed., Fractal Solutions for Understanding Complex Systems in Earth Sciences: Springer International Publishing, 1-18.

Fedi, M., and G. Florio, 2001, Detection of potential fields source boundaries by enhanced horizontal derivative method: Geophysical Prospecting, **49**, no. 1, 40-58. http://dx.doi.org/https://doi.org/10.1046/j.1365-2478.2001.00235.x.

Fedi, M., and G. Florio, 2002, A stable downward continuation by using the ISVD method*: Geophysical Journal International, **151**, no. 1, 146-156. http://dx.doi.org/10.1046/j.1365-246X.2002.01767.x.

Fedi, M., and G. Florio, 2006, SCALFUN: 3D analysis of potential field scaling function to determine independently or simultaneously Structural Index and depth to source, SEG Technical Program Expanded Abstracts 2006, 963-967.

Fedi, M., and G. Florio, 2009, The differential scaling function: A local estimator of source parameters of potential fields, SEG Technical Program Expanded Abstracts 2009, 918-922.

Fedi, M., and M. Pilkington, 2012, Understanding imaging methods for potential field data: GEOPHYSICS, **77**, no. 1, G13-G24.

Fedi, M., and G. Florio, 2013, Determination of the maximum-depth to potential field sources by a maximum structural index method: Journal of Applied Geophysics, **88**, 154-160. http://dx.doi.org/https://doi.org/10.1016/j.jappgeo.2012.10.009.

Fedi, M., V. Paoletti, and A. Rapolla. 2003, The role of multilevel data in potential field interpretation. Paper read at 8th SAGA Biennial Technical Meeting and Exhibition.

Fedi, M., P. C. Hansen, and V. Paoletti, 2005, Analysis of depth resolution in potential-field inversion: GEOPHYSICS, **70**, no. 6, A1-A11. http://dx.doi.org/10.1190/1.2122408.

Fedi, M., G. Florio, and T. A. M. Quarta, 2009, Multiridge analysis of potential fields: Geometric method and reduced Euler deconvolution: GEOPHYSICS, **74**, no. 4, L53-L65. http://dx.doi.org/10.1190/1.3142722.

Fedi, M., G. Florio, and V. Paoletti, 2015, MHODE: a local-homogeneity theory for improved source-parameter estimation of potential fields: Geophysical Journal International, **202**, no. 2, 887-900. http://dx.doi.org/10.1093/gji/ggv185.

Fehler, M., and P. J. Keliher, 2011, SEAM phase 1: Challenges of subsalt imaging in tertiary basins, with emphasis on deepwater Gulf of Mexico: Society of Exploration Geophysicists.

Filina, I., N. Delebo, G. Mohapatra, C. Coble, G. Harris, J. Layman, M. Strickler, and J.-P. Blangy, 2015, Integration of seismic and gravity data — A case study from the western Gulf of Mexico: Interpretation, **3**, no. 4, SAC99-SAC106. http://dx.doi.org/10.1190/int-2015-0050.1.

Florio, G., and M. Fedi, 2014, Multiridge Euler deconvolution: Geophysical Prospecting, **62**, no. 2, 333-351. http://dx.doi.org/https://doi.org/10.1111/1365-2478.12078.

Florio, G., M. Fedi, and F. Cella, 2022, A fractional vertical derivative technique for regional-residual separation: Geophysical Journal International, **232**, no. 1, 601-614. http://dx.doi.org/10.1093/gji/ggac348.

Fregoso, E., and L. A. Gallardo, 2009, Cross-gradients joint 3D inversion with applications to gravity and magnetic data: GEOPHYSICS, **74**, no. 4, L31-L42. http://dx.doi.org/10.1190/1.3119263.

Gallardo, L. A., and M. A. Meju, 2003, Characterization of heterogeneous near-surface materials by joint 2D inversion of dc resistivity and seismic data: Geophysical Research Letters, **30**, no. 13. http://dx.doi.org/https://doi.org/10.1029/2003GL017370.

Gallardo, L. A., and M. A. Meju, 2011, Structure-coupled multiphysics imaging in geophysical sciences: Reviews of Geophysics, **49**, no. 1. http://dx.doi.org/https://doi.org/10.1029/2010RG000330.

Gao, J., and H. Zhang, 2018, An efficient sequential strategy for realizing cross-gradient joint inversion: method and its application to 2-D cross borehole seismic traveltime and DC resistivity tomography: Geophysical Journal International, **213**, no. 2, 1044-1055. http://dx.doi.org/10.1093/gji/ggy026.

Gardner, G. H. F., L. W. Gardner, and A. R. Gregory, 1974, FORMATION VELOCITY AND DENSITY—THE DIAGNOSTIC BASICS FOR STRATIGRAPHIC TRAPS: GEOPHYSICS, **39**, no. 6, 770-780. http://dx.doi.org/10.1190/1.1440465.

Gerovska, D., P. Stavrev, and M. J. Araúzo-Bravo, 2005, Finite-difference Euler Deconvolution Algorithm Applied to the Interpretation of Magnetic Data from Northern Bulgaria: pure and applied geophysics, **162**, no. 3, 591-608. http://dx.doi.org/10.1007/s00024-004-2623-1.

Gonçalves, M. M., and E. P. Leite, 2019, Cooperative inversion of seismic reflection and gravity data: An object-based approach: Journal of Applied Geophysics, **167**, 42-50. http://dx.doi.org/https://doi.org/10.1016/j.jappgeo.2019.05.006.

Gross, L., 2019, Weighted cross-gradient function for joint inversion with the application to regional 3-D gravity and magnetic anomalies: Geophysical Journal International, **217**, no. 3, 2035-2046. http://dx.doi.org/10.1093/gji/ggz134.

Hansen, P. C., 1998, Rank-deficient and discrete ill-posed problems: numerical aspects of linear inversion: SIAM.

Herceg, M., I. M. Artemieva, and H. Thybo, 2015, Sensitivity analysis of crustal correction for calculation of lithospheric mantle density from gravity data: Geophysical Journal International, **204**, no. 2, 687-696. http://dx.doi.org/10.1093/gji/ggv431.

Huang, R., S. Liu, R. Qi, and Y. Zhang, 2021, Deep Learning 3D Sparse Inversion of Gravity Data: Journal of Geophysical Research: Solid Earth, **126**, no. 11, e2021JB022476. http://dx.doi.org/https://doi.org/10.1029/2021JB022476.

Ialongo, S., M. Fedi, and G. Florio, 2014, Invariant models in the inversion of gravity and magnetic fields and their derivatives: Journal of Applied Geophysics, **110**, 51-62. http://dx.doi.org/https://doi.org/10.1016/j.jappgeo.2014.07.023.

Jiang, W., 2020, 3-D joint inversion of seismic waveform and airborne gravity gradiometry data: Geophysical Journal International, **223**, no. 2, 746-764. http://dx.doi.org/10.1093/gji/ggaa296.

Kearey, P., M. Brooks, and I. Hill, 2002, An introduction to geophysical exploration. Vol. 4: John Wiley & Sons.

Kellogg, O. D., 1967, Foundations of potential theory. Vol. 31: Springer Science & Business Media.

LaFehr, T. R., and M. N. Nabighian, 2012, Fundamentals of Gravity Exploration: Society of Exploration Geophysicists.

LaFehr, T. R., V. C. Dean, T. L. Davis, and F. J. Hilterman, 1983, Seismic and gravity modeling of the mors salt dome, Denmark, SEG Technical Program Expanded Abstracts 1983, 301-303.

Last, B. J., and K. Kubik, 1983, Compact gravity inversion: GEOPHYSICS, **48**, no. 6, 713-721. http://dx.doi.org/10.1190/1.1441501.

Lelièvre, P. G., C. G. Farquharson, and C. A. Hurich, 2012, Joint inversion of seismic traveltimes and gravity data on unstructured grids with application to mineral exploration: Geophysics, **77**, no. 1, K1-K15. http://dx.doi.org/10.1190/geo2011-0154.1.

Li, Y., 2001, 3‐D inversion of gravity gradiometer data, SEG Technical Program Expanded Abstracts 2001, 1470-1473.

Li, Y., and D. W. Oldenburg, 1996, 3-D inversion of magnetic data: GEOPHYSICS, **61**, no. 2, 394-408.

Li, Y., and D. W. Oldenburg, 1998, 3-D inversion of gravity data: GEOPHYSICS, **63**, no. 1, 109-119.

Li, Y., and D. W. Oldenburg, 2000, Joint inversion of surface and three‐component borehole magnetic data: GEOPHYSICS, **65**, no. 2, 540-552. http://dx.doi.org/10.1190/1.1444749.
Lines, L. R., A. K. Schultz, and S. Treitel, 1988, Cooperative inversion of geophysical data: GEOPHYSICS, **53**, no. 1, 8-20. http://dx.doi.org/10.1190/1.1442403.
Litinsky, V. A., 1989a, Concept of effective density: Key to gravity depth determinations for sedimentary basins: GEOPHYSICS, **54**, no. 11, 1474-1482. http://dx.doi.org/10.1190/1.1442611.
Litinsky, V. A., 1989b, Concept of effective density; key to gravity depth determinations for sedimentary basins: GEOPHYSICS, **54**, no. 11, 1474-1482. http://dx.doi.org/10.1190/1.1442611.
Liu, S., J. Baniamerian, and M. Fedi, 2020, Imaging Methods Versus Inverse Methods: An Option or An Alternative?: IEEE Transactions on Geoscience and Remote Sensing, **58**, no. 5, 3484-3494. http://dx.doi.org/10.1109/TGRS.2019.2957412.
Liu, S., X. Hu, M. Fedi, J. Baniamerian, M. A. Abbas, and M. S. Chauhan, 2024, Petrophysical and geophysical constrained inversion of gravity data based on starting and referenced models: Journal of Geophysics and Engineering. http://dx.doi.org/10.1093/jge/gxae111.
Lofi, J., J. Déverchère, V. Gaullier, H. Gillet, C. Gorini, P. Guennoc, L. Loncke, A. Maillard, F. Sage, and I. Thinon, 2011, Seismic atlas of the Messinian Salinity Crisis markers in the Mediterranean and Black Seas. Vol. 179: Société Géologique de France.
Ludwig, W. J., 1971, 2. SEISMIC REFRACTION (May 1968) WILLIAM J. LUDWIG, JOHN E. NAFE, AND CHARLES L. DRAKE 1. Introduction The seismic refraction method provides us with a means of determining the: The sea, ideas and observations on progress in the study of the seas, **4**, 53.
Maiolino, M., and M. Fedi, 2022, Excess Mass from Dexp Transformation of the Gravity Field, **2022**, no. 1, 1-5. http://dx.doi.org/https://doi.org/10.3997/2214-4609.202210819.
Marfurt, K. J., and T. M. Alves, 2015, Pitfalls and limitations in seismic attribute interpretation of tectonic features: Interpretation, **3**, no. 1, SB5-SB15. http://dx.doi.org/10.1190/int-2014-0122.1.
Martínez-Moreno, F., A. Pedrera, J. Galindo-Zaldívar, M. López-Chicano, A. Azor, W. Martín-Rosales, P. Ruano, J. Calaforra, and A. Hódar-Pérez, 2016, The Gruta de las Maravillas (Aracena, South-West Iberia): Setting and origin of a cave in marbles from dissolution of pyrite: Geomorphology, **253**, 239-250.
Martínez-Moreno, F., J. Galindo-Zaldívar, A. Pedrera, T. Teixido, P. Ruano, J. Peña, L. González-Castillo, A. Ruiz-Constán, M. López-Chicano, and W. Martín-Rosales, 2014, Integrated geophysical methods for studying the karst system of Gruta de las Maravillas (Aracena, Southwest Spain): Journal of Applied Geophysics, **107**, 149-162.
Martinez, C., and Y. Li, 2011, Inversion of regional gravity gradient data over the Vredefort Impact Structure, South Africa, SEG Technical Program Expanded Abstracts 2011, 841-845.
Meng, Q., G. Ma, L. Li, T. Wang, and J. Han, 2022, 3-D Cross-Gradient Joint Inversion Method for Gravity and Magnetic Data With Unstructured Grids Based on Second-Order Taylor Formula: Its Application to the Southern Greater Khingan Range: IEEE Transactions on Geoscience and Remote Sensing, **60**, 1-16. http://dx.doi.org/10.1109/TGRS.2022.3172337.
Menke, W., 2018, Geophysical data analysis: Discrete inverse theory: Academic press.
Milano, M., Y. Kelemework, M. La Manna, M. Fedi, D. Montanari, and M. Iorio, 2020, Crustal structure of Sicily from modelling of gravity and magnetic anomalies: Scientific Reports, **10**, no. 1, 16019.
Moorkamp, M., B. Heincke, M. Jegen, A. W. Roberts, and R. W. Hobbs, 2011, A framework for 3-D joint inversion of MT, gravity and seismic refraction data: Geophysical Journal International, **184**, no. 1, 477-493. http://dx.doi.org/10.1111/j.1365-246X.2010.04856.x.
Nafe, J. E., and C. L. Drake, 1957, VARIATION WITH DEPTH IN SHALLOW AND DEEP WATER MARINE SEDIMENTS OF POROSITY, DENSITY AND THE VELOCITIES OF

COMPRESSIONAL AND SHEAR WAVES: GEOPHYSICS, **22**, no. 3, 523-552. http://dx.doi.org/10.1190/1.1438386.

Paoletti, V., S. Ialongo, G. Florio, M. Fedi, and F. Cella, 2013, Self-constrained inversion of potential fields: Geophysical Journal International, **195**, no. 2, 854-869. http://dx.doi.org/10.1093/gji/ggt313.

Paoletti, V., M. Fedi, F. Italiano, G. Florio, and S. Ialongo, 2016, Inversion of gravity gradient tensor data: does it provide better resolution?: Geophysical Journal International, **205**, no. 1, 192-202. http://dx.doi.org/10.1093/gji/ggw003.

Parasnis, D., 1975, Mining geophysics. Vol. 3: Elsevier.

Parker, R. L., 1977, Understanding inverse theory: Annual Review of Earth and Planetary Sciences, Vol. 5, p. 35, **5**, 35.

Pilkington, M., 2009, 3D magnetic data-space inversion with sparseness constraints: GEOPHYSICS, **74**, no. 1, L7-L15. http://dx.doi.org/10.1190/1.3026538.

Portniaguine, O., and M. S. Zhdanov, 1999, Focusing geophysical inversion images: GEOPHYSICS, **64**, no. 3, 874-887. http://dx.doi.org/10.1190/1.1444596.

Portniaguine, O., and M. S. Zhdanov, 2002, 3‐D magnetic inversion with data compression and image focusing: GEOPHYSICS, **67**, no. 5, 1532-1541. http://dx.doi.org/10.1190/1.1512749.

Reid, A. B., J. M. Allsop, H. Granser, A. J. Millett, and I. W. Somerton, 1990, Magnetic interpretation in three dimensions using Euler deconvolution: GEOPHYSICS, **55**, no. 1, 80-91. http://dx.doi.org/10.1190/1.1442774.

Reynolds, J. M., 2011, An introduction to applied and environmental geophysics: John Wiley & Sons.

Roveri, M., R. Flecker, W. Krijgsman, J. Lofi, S. Lugli, V. Manzi, F. J. Sierro, A. Bertini, A. Camerlenghi, and G. De Lange, 2014, The Messinian Salinity Crisis: past and future of a great challenge for marine sciences: Marine Geology, **352**, 25-58.

Roy, A., 1962, AMBIGUITY IN GEOPHYSICAL INTERPRETATION: GEOPHYSICS, **27**, no. 1, 90-99. http://dx.doi.org/10.1190/1.1438985.

Sampietro, D., and M. Capponi, 2021, Seismic Constrained Gravity Inversion: A Reliable Tool to Improve Geophysical Models Away from Seismic Information: Geosciences, **11**, no. 11, 467. https://www.mdpi.com/2076-3263/11/11/467.

Scandone, P., G. Giunta, and V. Liguori, 1975, THE CONNECTION BETWEEN THE APULIA AND THE SAHARA CONTINENTAL MARGINS IN THE SOUTHERN APENNINES AND IN SICILY.

Sgroi, T., R. de Nardis, and G. Lavecchia, 2012, Crustal structure and seismotectonics of central Sicily (southern Italy): new constraints from instrumental seismicity: Geophysical Journal International, **189**, no. 3, 1237-1252.

Shi, X., Z. Jia, H. Geng, S. Liu, and Y. Li, 2023, Deep Learning Inversion for Multivariate Magnetic Data: IEEE Transactions on Geoscience and Remote Sensing.

Silva, J. B. C., W. E. Medeiros, and V. C. F. Barbosa, 2001, Potential‐field inversion: Choosing the appropriate technique to solve a geologic problem: GEOPHYSICS, **66**, no. 2, 511-520. http://dx.doi.org/10.1190/1.1444941.

Skeels, D. C., 1947, AMBIGUITY IN GRAVITY INTERPRETATION: GEOPHYSICS, **12**, no. 1, 43-56. http://dx.doi.org/10.1190/1.1437295.

Smith, R. A., 1959, SOME DEPTH FORMULAE FOR LOCAL MAGNETIC AND GRAVITY ANOMALIES: Geophysical Prospecting, **7**, no. 1, 55-63. http://dx.doi.org/https://doi.org/10.1111/j.1365-2478.1959.tb01453.x.

Stavrev, P. Y., 1997, Euler deconvolution using differential similarity transformations of gravity or magnetic anomalies[Link]: Geophysical Prospecting, **45**, no. 2, 207-246. http://dx.doi.org/https://doi.org/10.1046/j.1365-2478.1997.00331.x.

Sun, J., and Y. Li, 2016, Joint inversion of multiple geophysical data using guided fuzzy c-means clustering: GEOPHYSICS, **81**, no. 3, ID37-ID57. http://dx.doi.org/10.1190/geo2015-0457.1.

Tavakoli, M., A. Nejati Kalateh, M. Rezaie, L. Gross, and M. Fedi, 2021, Sequential joint inversion of gravity and magnetic data via the cross‐gradient constraint: Geophysical Prospecting, **69**, no. 7, 1542-1559. http://dx.doi.org/https://doi.org/10.1111/1365-2478.13120.

Tikhonov, A. N., V. J. Arsenin, V. I. A. k. Arsenin, and V. Y. Arsenin, 1977, Solutions of ill-posed problems: Vh Winston.

Tzevahirtzian, A., A. Caruso, F. Andreetto, S. Bonomo, and W. Krijgsman, 2023, A bio-chronostratigraphic study of the upper Miocene from the northern Caltanissetta Basin, Sicily (core 3AGN2S04). Implications for dating the Messinian Salinity Crisis onset: Sedimentary Geology, **445**, 106330.

Um, E. S., M. Commer, and G. A. Newman, 2014, A strategy for coupled 3D imaging of large-scale seismic and electromagnetic data sets: Application to subsalt imaging: GEOPHYSICS, **79**, no. 3, ID1-ID13. http://dx.doi.org/10.1190/geo2013-0053.1.

Vatankhah, S., S. Liu, R. A. Renaut, X. Hu, J. D. Hogue, and M. Gharloghi, 2022, An Efficient Alternating Algorithm for the L_p-Norm Cross-Gradient Joint Inversion of Gravity and Magnetic Data Using the 2-D Fast Fourier Transform: IEEE Transactions on Geoscience and Remote Sensing, **60**, 1-16. http://dx.doi.org/10.1109/TGRS.2020.3033043.

Vitale, A., and M. Fedi, 2020, Self-constrained inversion of potential fields through a 3D depth weighting: GEOPHYSICS, **85**, no. 6, G143-G156. http://dx.doi.org/10.1190/geo2019-0812.1.

Vitale, A., G. Gabbriellini, and M. Fedi, 2023, Deep learning to estimate the basement depth by gravity data using a feedforward neural network: GEOPHYSICS, **88**, no. 3, G95-G103. http://dx.doi.org/10.1190/geo2022-0201.1.

Wang, C., and Z. Xu, 2021, An intelligent fault diagnosis model based on deep neural network for few-shot fault diagnosis: Neurocomputing, **456**, 550-562.

Yilmaz, Ö., 2001, Seismic Data Analysis, Seismic Data Analysis: Society of Exploration Geophysicists.

Yu, P., J. L. Wang, J. S. Wu, and D. W. Wang, 2007, Constrained joint inversion of gravity and seismic data using the simulated annealing algorithm: Chinese Journal of Geophysics, **50**, no. 2, 465-475.

Zhang, R., T. Li, and C. Liu, 2021, Joint inversion of multiphysical parameters based on a combination of cosine dot-gradient and joint total variation constraints: IEEE Transactions on Geoscience and Remote Sensing, **60**, 1-10.

Zhang, S., C. Yin, X. Cao, S. Sun, Y. Liu, and X. Ren, 2022, DecNet: Decomposition network for 3D gravity inversion: GEOPHYSICS, **87**, no. 5, G103-G114.

Zhang, Y., and Y. Wang, 2019, THREE-DIMENSIONAL GRAVITY-MAGNETIC CROSS-GRADIENT JOINT INVERSION BASED ON STRUCTURAL COUPLING AND A FAST GRADIENT METHOD: Journal of Computational Mathematics, **37**, no. 6.

Zhdanov, M. S., R. Ellis, and S. Mukherjee, 2004, Three‐dimensional regularized focusing inversion of gravity gradient tensor component data: GEOPHYSICS, **69**, no. 4, 925-937. http://dx.doi.org/10.1190/1.1778236.